

# Critical role of ATP-induced ATP release for $\text{Ca}^{2+}$ signaling in nonsensory cell networks of the developing cochlea

 Federico Ceriani<sup>a,b,c,1</sup>, Tullio Pozzan<sup>d,e,2</sup>, and Fabio Mammano<sup>a,b,c,f,2</sup>

<sup>a</sup>Department of Biomedical Sciences, Institute of Cell Biology and Neurobiology, Italian National Research Council, 00015 Monterotondo (RM), Italy; <sup>b</sup>Department of Physics and Astronomy, University of Padua, 35131 Padua, Italy; <sup>c</sup>Connexin Structure and Function Unit, Venetian Institute of Molecular Medicine, Foundation for Advanced Biomedical Research, 35129 Padua, Italy; <sup>d</sup>Department of Biomedical Sciences, Institute of Neuroscience (Padua Section), Italian National Research Council, 35121 Padua, Italy; <sup>e</sup>Department of Biomedical Sciences, University of Padua, 35121 Padua, Italy; and <sup>f</sup>Laboratory of Phenotypic Screening, Shanghai Institute for Advanced Immunochemical Studies, ShanghaiTech University, Shanghai 201210, China

Contributed by Tullio Pozzan, October 1, 2016 (sent for review July 5, 2016; reviewed by Gary D. Housley and Luc Leybaert)

**Spatially and temporally coordinated variations of the cytosolic free calcium concentration ( $[\text{Ca}^{2+}]_c$ ) play a crucial role in a variety of tissues. In the developing sensory epithelium of the mammalian cochlea, elevation of extracellular adenosine triphosphate concentration ( $[\text{ATP}]_e$ ) triggers  $[\text{Ca}^{2+}]_c$  oscillations and propagation of intercellular inositol 1,4,5-trisphosphate ( $\text{IP}_3$ )-dependent  $\text{Ca}^{2+}$  waves. What remains uncertain is the relative contribution of gap junction channels and connexin hemichannels to these fundamental mechanisms, defects in which impair hearing acquisition. Another related open question is whether  $[\text{Ca}^{2+}]_c$  oscillations require oscillations of the cytosolic  $\text{IP}_3$  concentration ( $[\text{IP}_3]_c$ ) in this system. To address these issues, we performed  $\text{Ca}^{2+}$  imaging experiments in the lesser epithelial ridge of the mouse cochlea around postnatal day 5 and constructed a computational model in quantitative adherence to experimental data. Our results indicate that  $[\text{Ca}^{2+}]_c$  oscillations are governed by Hopf-type bifurcations within the experimental range of  $[\text{ATP}]_e$  and do not require  $[\text{IP}_3]_c$  oscillations. The model replicates accurately the spatial extent and propagation speed of intercellular  $\text{Ca}^{2+}$  waves and predicts that ATP-induced ATP release is the primary mechanism underlying intercellular propagation of  $\text{Ca}^{2+}$  signals. The model also uncovers a discontinuous transition from propagating regimes (intercellular  $\text{Ca}^{2+}$  wave speed  $> 11 \mu\text{m}\cdot\text{s}^{-1}$ ) to propagation failure (speed = 0), which occurs upon lowering the maximal ATP release rate below a minimal threshold value. The approach presented here overcomes major limitations due to lack of specific connexin channel inhibitors and can be extended to other coupled cellular systems.**

inositol trisphosphate | calcium waves | calcium oscillations | cochlear nonsensory cells | connexins

In the mammalian cochlea, sensory hair cells perform mechanotransduction, i.e., the conversion of sound-evoked mechanical stimuli into electrical signals that are conveyed to the central nervous system along the fibers of the auditory nerve (1). Unlike normal human newborns that hear at birth, most rodents start hearing at postnatal days 10–14 (P10–P14, where P0 is day of birth) and achieve adult-level auditory thresholds by the third postnatal week (2). Preceding the acquisition of hearing, the highly specialized and polarized sensory epithelium of the murine cochlea comprises the greater epithelial ridge, from which inner hair cells and medial nonsensory cells originate, and the adjacent lesser epithelial ridge, which is presumed to generate outer hair cells and lateral nonsensory cells (3, 4). Several of these cells express a glial marker (5).

Purinergic signaling, which is key to cochlear physiology and pathology (6–8), promotes cytosolic free calcium concentration ( $[\text{Ca}^{2+}]_c$ ) oscillations and intercellular  $\text{Ca}^{2+}$  waves in the matrix of gap-junction-coupled nonsensory cells (9) that embed the sensory inner and outer hair cells of the organ of Corti (2). In this cellular system, a host of experimental data (10, 11) indicate that extracellular ATP binding to G-protein-coupled P2Y receptors activates a canonical transduction

cascade whereby phospholipase C (PLC)-dependent hydrolysis of phosphatidylinositol 4,5-bisphosphate ( $\text{PIP}_2$ ) generates the second-messenger inositol 1,4,5-trisphosphate ( $\text{IP}_3$ ) and diacylglycerol (12). When  $\text{IP}_3$  binds to and opens intracellular receptors ( $\text{IP}_3\text{R}$ ), it triggers  $\text{Ca}^{2+}$  release from the endoplasmic reticulum (ER) and raises the  $[\text{Ca}^{2+}]_c$  (12). Phosphatidylinositol phosphate kinase type 1 $\gamma$  ( $\text{PIP}1\gamma$ ) is the enzyme that is primarily responsible for the synthesis of the  $\text{IP}_3$  precursor  $\text{PIP}_2$  in the cochlea (13).

Connexins participate in this sequence of events as follows: (i) as gap junction channels, composed of connexins 26 and 30 (14–17), which enable  $\text{IP}_3$  movement between coupled cells of the organ of Corti (18); (ii) as connexin hemichannels in the cell plasma membrane (19, 20), which mediate paracrine signaling by opening in response to a raised level of the  $[\text{Ca}^{2+}]_c$  (21–23); and (iii) these hemichannels release intracellular ATP to the extracellular milieu, whereas ATP degradation by ectonucleotidases terminates this purinergic signaling (19, 20). Altogether, these concerted molecular mechanisms promote encoding of signals by  $[\text{Ca}^{2+}]_c$  oscillations (24, 25) and convey crucial biochemical information to every district of the cochlear sensory epithelium via intercellular  $\text{Ca}^{2+}$  waves (2, 26).

## Significance

**This study dissects the mechanisms underlying the occurrence of ATP- and inositol 1,4,5-trisphosphate ( $\text{IP}_3$ )-dependent intracellular cytosolic free calcium concentration  $[\text{Ca}^{2+}]_c$  oscillations and intercellular  $\text{Ca}^{2+}$  waves in the syncytium formed by nonsensory cells in the postnatal mouse cochlea. The findings are significant with regard to development of the cochlear sensory epithelium, injury signaling in the cochlea, and pathophysiology around connexinopathies that dominate prelingual deafness. On a broader frame, this work provides an accurate, quantitative description of the mode of propagation of extracellular ATP-mediated paracrine signaling in epithelial cells. Critically, the modeling brings together a synthesis of quantitative data on the key elements concerning the signaling molecules (ATP and  $\text{IP}_3$ ) and propagation mechanisms from a broad range of prior work.**

Author contributions: F.C., T.P., and F.M. designed research; F.C. performed research; F.C. analyzed data; and T.P. and F.M. wrote the paper.

Reviewers: G.D.H., University of New South Wales; and L.L., Ghent University.

The authors declare no conflict of interest.

Freely available online through the PNAS open access option.

<sup>1</sup>Present address: Department of Biomedical Science, University of Sheffield, Sheffield S10 2TN, United Kingdom.

<sup>2</sup>To whom correspondence may be addressed. Email: tullio.pozzan@unipd.it or fabio.mammano@cnr.it.

This article contains supporting information online at [www.pnas.org/lookup/suppl/doi:10.1073/pnas.1616061113/-DCSupplemental](http://www.pnas.org/lookup/suppl/doi:10.1073/pnas.1616061113/-DCSupplemental).

Prior work with mouse cochlear organotypic cultures indicates that  $[Ca^{2+}]_c$  oscillations and  $Ca^{2+}$  waves in cochlear nonsensory cells of both the lesser (10, 11) and the greater epithelial ridge (27, 28) (Fig. S1) share the same PLC- and  $IP_3$ R-dependent signal transduction cascade activated by ATP (13). This signaling cascade has been implicated in the sensing of noise-induced hearing loss (10), as well as in developmental defects that impair hearing acquisition due to genetic mutations in key components of the cascade (13, 18, 28). However, the relative contribution of connexin hemichannels and intercellular gap junction channels has not been determined, due to lack of specific inhibitors acting selectively on one of the two types of channels made by connexins (29). Another related open question that is difficult to address experimentally in this native tissue is whether oscillations in  $IP_3$  concentration ( $[IP_3]_c$ ) are an obligatory component of  $[Ca^{2+}]_c$  oscillations (30–33).

In this study, we present a data-driven computational model designed to address these unresolved issues. We show that the occurrence of  $[Ca^{2+}]_c$  oscillations within a well-defined range of extracellular adenosine triphosphate concentration ( $[ATP]_e$ ) (10, 11) can be described in terms of Hopf-type bifurcations (34). In addition, we quantify precisely the contribution of  $IP_3$  diffusion through gap junction channels and paracrine signaling mediated by ATP release through connexin hemichannels to the propagation of intercellular  $Ca^{2+}$  signals. Our experimental results are consistent with a model whereby  $Ca^{2+}$  oscillations do not require  $IP_3$  oscillations and can develop in the presence of an elevated and stable background of  $IP_3$ .

## Results

**$[Ca^{2+}]_c$  Oscillations Do Not Require  $[IP_3]_c$  Oscillations and Are Governed by Hopf-Type Bifurcations.** It is well known that  $[Ca^{2+}]_c$  can be modulated by a variety of mechanisms, including  $Ca^{2+}$  release from various intracellular stores and influx from the extracellular space (25). However, in the present as well as the majority of our previously published work, we focused on purinergic signaling at the endolymphatic surface of the sensory epithelium around P5. Endolymph, which fills the cochlear duct (scala media) and bathes the apical surface of both sensory and nonsensory cells, is an unusual extracellular fluid characterized by a positive potential, known as the endocochlear potential (35). Moreover, endolymph contains high levels of  $K^+$  and  $Cl^-$ , low levels of  $Na^+$  (36), and an extremely low extracellular free  $Ca^{2+}$  concentration ( $[Ca^{2+}]_o$ ) (37). In mice at P5, the endocochlear potential is still negligible, whereas the endolymphatic ion concentrations reach almost adult levels (38). Our experiments with cochlear organotypic cultures obtained from P5 mice were conducted in low, endolymph-like  $[Ca^{2+}]_o$  (20  $\mu M$ ), a condition in which  $Ca^{2+}$  influx is reduced to a minimum. In fact,  $[Ca^{2+}]_c$  oscillations evoked by extracellular ATP in cochlear nonsensory cells of the lesser epithelial ridge (10, 11, 13, 19, 20), as well as spontaneous  $Ca^{2+}$  transients in the greater epithelial ridge (13, 28), persisted for tens of minutes in 20  $\mu M$   $[Ca^{2+}]_o$  or even in a divalent-free extracellular medium. Therefore, in constructing the model represented in Fig. 1 and described in *Supporting Information*, we neglected  $Ca^{2+}$  exchange through the plasma membrane [including the basolateral plasma membrane that in vivo is exposed to ordinary  $[Ca^{2+}]_o$  levels and contains elements of the  $Ca^{2+}$  entry pathway, such as TRPC channels (39)], effectively reducing our stereotyped cell to a closed compartment in which the total intracellular  $[Ca^{2+}]_o$  is constant. In addition, based on the insensitivity of cochlear nonsensory cells to caffeine (11) and akin to similar models of  $Ca^{2+}$  dynamics in nonexcitable cells (32, 33), we considered  $IP_3$ -dependent  $Ca^{2+}$  release from the ER as the only mechanism responsible for the observed  $[Ca^{2+}]_c$  increase. Finally, to fine-tune model parameters (Table S1) we performed a variety of  $Ca^{2+}$  imaging experiments in apical cochlear cultures from P5 mice and iteratively compared model predictions to experimental results, as detailed hereafter.

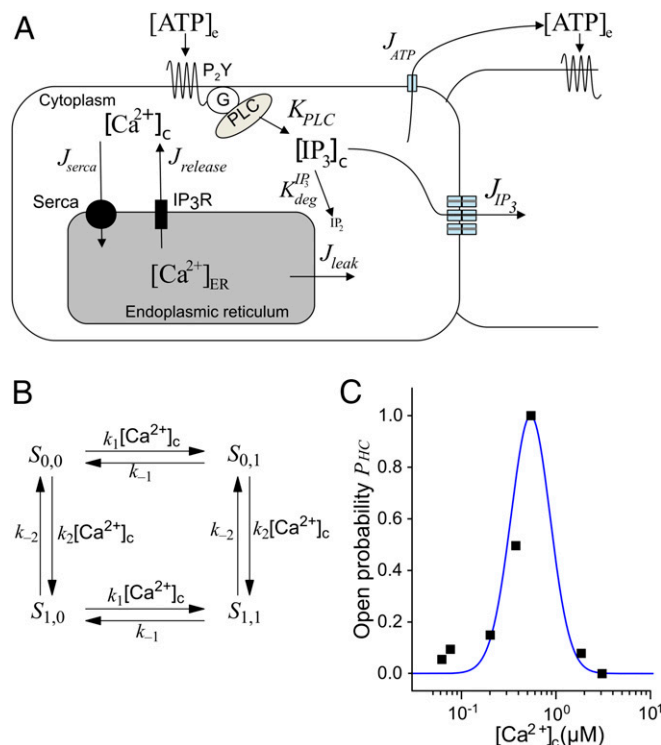


**Fig. 1.** Components of the computational model of  $Ca^{2+}$  dynamics in cochlear nonsensory cells. (A) Schematic representation of the model. Letters  $J$  and  $K$  indicate fluxes through channels/pumps and rate of production/degradation, respectively (all in  $\mu M \cdot s^{-1}$ ). (B) Four-state model of a connexin hemichannel. (C) Hemichannel open probability as a function of  $[Ca^{2+}]_c$ . Black squares, data from ref. 22; blue solid line, fit generated by the model in B.

In a first set of experiments (Fig. 2), we stimulated cochlear nonsensory cells of the lesser epithelial ridge by the steady pressure application of ATP from a glass micropipette.  $[Ca^{2+}]_c$  oscillations were detected only within a limited range of ATP concentrations, consistent with previous reports (10, 11). Specifically,  $[Ca^{2+}]_c$  responses failed to exhibit an oscillatory character at  $[ATP]_e < 10$  nM (two cultures for each concentration). Small-amplitude, damped  $[Ca^{2+}]_c$  oscillations were detected between  $\sim 20$  nM and 50 nM  $[ATP]_e$  (three cultures for each concentration). Sizeable, self-sustained  $[Ca^{2+}]_c$  oscillations could be reliably elicited in nine of nine organotypic cultures for  $[ATP]_e$  in the concentration range from 50 nM to 1  $\mu M$ . Above this  $[ATP]_e$  value, oscillations displayed again a damped (or overdamped) character and  $[Ca^{2+}]_c$  returned to baseline in 40–110 s, probably due to a combination of P2Y receptor desensitization (40) and limiting factors affecting G proteins or PLC function.

$[Ca^{2+}]_c$  responses in the computational model replicated experimental data (Fig. 2A) and fitted the ATP dose–response curve for the peak ATP-evoked  $[Ca^{2+}]_c$  over the whole range of tested  $[ATP]_e$  (Fig. 2B). Analysis of the model results suggests that (i) for  $[ATP]_e$  between approximately 50 nM and 1  $\mu M$ , self-sustained  $[Ca^{2+}]_c$  oscillations in cochlear nonsensory cells can develop in the presence of an elevated and stable background of  $[IP_3]_c$ ; (ii) for  $[ATP]_e$  in excess of  $\sim 1$   $\mu M$ , after an initial  $[IP_3]_c$  surge, P2Y receptor desensitization combines with  $IP_3$  degradation, causing an exponential fall of  $[IP_3]_c$  over time. We performed a computational analysis based on bifurcation theory (41) and determined that the appearance and disappearance of  $[Ca^{2+}]_c$  oscillations are governed by supercritical Hopf bifurcations (34) occurring at  $\sim 0.055$   $\mu M$  and  $\sim 0.745$   $\mu M$   $[ATP]_e$  (Fig. 3).

In our computational model, the occurrence of  $[Ca^{2+}]_c$  oscillations (blue traces in Fig. 2A) is due to the interplay of (i)  $IP_3$ -dependent  $Ca^{2+}$  release from the ER; (ii)  $[Ca^{2+}]_c$  regulation of  $IP_3$  receptors

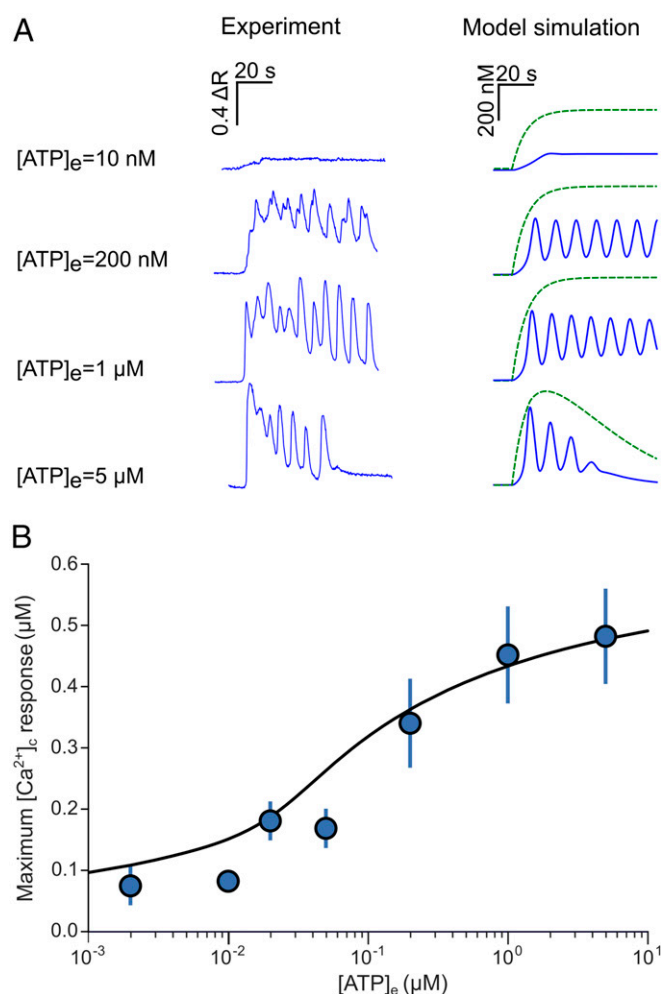


**Fig. 2.** ATP-evoked  $\text{Ca}^{2+}$  oscillations: comparison between experiments and simulations. (A) Representative traces recorded from individual nonsensory cells (Left) and corresponding model simulations (Right) for three different  $[\text{ATP}]_e$ s; blue traces are for  $[\text{Ca}^{2+}]_c$  and green for  $[\text{IP}_3]_c$ . (B)  $\text{Ca}^{2+}$  dose-response curve for ATP. Each data point represents the average peak  $[\text{Ca}^{2+}]_c$  response of at least 30 nonsensory cells in three different cochlear organotypic cultures; solid line shows model fit to the data.

(42), with  $\text{Ca}^{2+}$  promoting receptor opening at low concentrations but inhibiting it as its levels increase (43); and (iii)  $\text{Ca}^{2+}$  uptake into the ER by sarco/endoplasmic reticulum  $\text{Ca}^{2+}$ -ATPase (SERCA pumps). An important consequence is that  $[\text{Ca}^{2+}]_c$  oscillations may occur in the presence of  $[\text{IP}_3]_c$  responses that either are stationary or fail to display an oscillatory character (dashed green traces in Fig. 2A).

To corroborate this conclusion we used a  $\text{Ca}^{2+}$  imaging assay based on eliciting  $[\text{Ca}^{2+}]_c$  oscillations by ATP application followed by photostimulation with caged  $\text{IP}_3$ , to increase the  $[\text{IP}_3]_c$  at a specific time point (32). An increase in the oscillation frequency is expected if  $[\text{Ca}^{2+}]_c$  oscillations do not depend on  $[\text{IP}_3]_c$  oscillations. Conversely, a delay in the occurrence of the first  $[\text{Ca}^{2+}]_c$  peak after  $\text{IP}_3$  uncaging is expected if  $[\text{Ca}^{2+}]_c$  oscillations require (i.e., are driven by)  $[\text{IP}_3]_c$  oscillations through feedback regulation of  $\text{IP}_3$  production or degradation (32). To perform this assay, we coloaded cochlear organotypic cultures with Fluo-4 and caged  $\text{IP}_3$  and pressure-applied ATP (200 nM) from a glass micropipette positioned above the sensory epithelium while imaging Fluo-4 fluorescence. Forty seconds after starting ATP application, we activated a 365-nm light-emitting diode for 400 ms to stimulate all cells in the field of view by the uncaging of  $\text{IP}_3$ .

After  $\text{IP}_3$  photoactivation, (i) we always detected a significant, nearly twofold, increase in the frequency of  $[\text{Ca}^{2+}]_c$  oscillations (29 cells in  $n = 3$  cultures;  $P = 0.03$ , Mann-Whitney  $u$  test), and (ii) no delay was observed in the occurrence of the first  $[\text{Ca}^{2+}]_c$  peak (Fig. 4).

These results confirm that  $[\text{Ca}^{2+}]_c$  oscillations in this system do not require  $[\text{IP}_3]_c$  oscillations (32), in agreement with our model predictions (Fig. 2A). However, it might be of some interest to predict what would happen in the case that  $[\text{Ca}^{2+}]_c$  oscillations had to rely on  $[\text{IP}_3]_c$  oscillations (Figs. S2–S4). Changing three parameters (amplitude, frequency, and tonic component of  $[\text{IP}_3]_c$  oscillations) in a nonsystematic way showed that, at low frequency (0.1 Hz),  $[\text{Ca}^{2+}]_c$  oscillations would follow faithfully  $[\text{IP}_3]_c$  oscillations, albeit with a systematic delay (Fig. S2). Upon raising the frequency (0.5 Hz), the  $[\text{Ca}^{2+}]_c$  signal would track the  $[\text{IP}_3]_c$  phasic component only provided  $[\text{IP}_3]_c$  oscillations started from  $[\text{IP}_3]_c = 0$ . In the unlikely event that  $[\text{IP}_3]_c$  oscillated at a frequency of 2 Hz, the  $[\text{Ca}^{2+}]_c$  signal would be unable to keep the pace. Indeed,  $[\text{IP}_3]_c$  oscillations at both 0.5 Hz (Fig. S3) and 2 Hz (Fig. S4) would drive  $[\text{Ca}^{2+}]_c$  oscillations with variable degrees of damping and a frequency close to 0.1 Hz, which is the natural oscillation frequency of  $[\text{Ca}^{2+}]_c$  oscillations in the model.

### The Computational Model Replicates Range and Speed of Intercellular $\text{Ca}^{2+}$ Wave Propagation.

**Waves initiated by  $\text{IP}_3$  uncaging.** Having characterized and modeled  $\text{Ca}^{2+}$  dynamics at the single-cell level, we tackled the problem of intercellular signaling (26). Also in this case we used cochlear cultures coloaded with the AM ester forms of caged  $\text{IP}_3$  and of Fluo-4. However, for these experiments  $\text{Ca}^{2+}$  responses in the lesser epithelial ridge were evoked by a brief (170 ms) and focalized pulse of UV light. The irradiated area comprised a central cell and its six nearest neighbors from which radial  $\text{Ca}^{2+}$  waves propagated to  $18 \pm 1$  cells of the culture ( $n = 4$  experiments in three cultures) (Fig. 5). Similar waves were also evoked by photostimulation with caged  $\text{IP}_3$  in the greater epithelial ridge (13). To compare model predictions to experimental results, we reconstructed cell network topology by laser scanning confocal imaging (Fig. S1). All cells in the model were attributed a volume  $V = 3,900 \mu\text{m}^3$  (average estimate from our confocal images) whereas the unitary permeability to  $\text{IP}_3$  was set at  $p_u = 72 \times 10^{-3} \mu\text{m}^3 \cdot \text{s}^{-1}$  from ref. 44. Then, based on realistic cell network topology, we imposed an in silico sudden increase of  $[\text{IP}_3]_c$  in a group of neighboring cells (5  $\mu\text{M}$  in one cell and 0.7  $\mu\text{M}$  in its nearest neighbors, reflecting the different intensities of laser

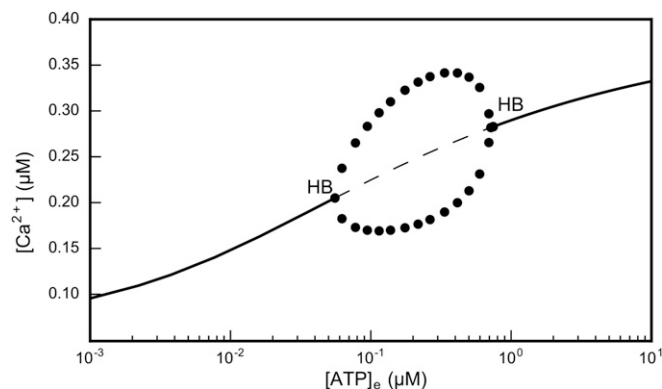


**Fig. 3.** Bifurcation diagram generated by the computational model. The solid and the dashed lines indicate, respectively, stable and unstable solutions of the system of differential equations described in Supporting Information. Circles indicate the amplitude of steady-state oscillations. The appearance and disappearance of self-sustained  $[\text{Ca}^{2+}]_c$  oscillations are determined by two supercritical Hopf bifurcations (HB) at  $[\text{ATP}]_e \approx 0.055 \mu\text{M}$  and  $[\text{ATP}]_e \approx 0.745 \mu\text{M}$ .

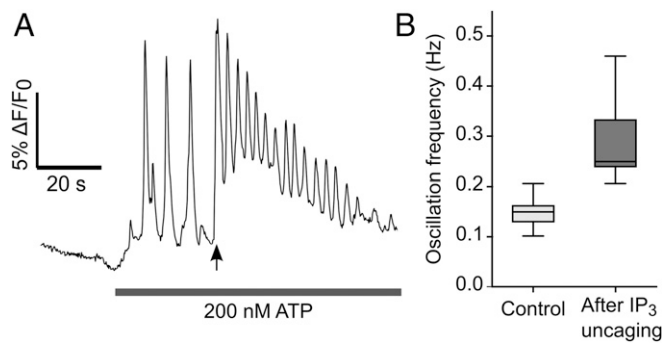


**Fig. 4.**  $\text{Ca}^{2+}$  imaging assay to confirm that  $\text{Ca}^{2+}$  oscillations do not require  $\text{IP}_3$  oscillations. (A) Representative fluorescence trace from a cochlear nonsensory cell during the application of the protocol detailed in ref. 32. After a baseline recording of 20 s, ATP (200 nM) was applied for the duration of the experiment. The solid arrow indicates  $\text{IP}_3$  photoactivation by a pulse of UV light. (B) Box plot summarizing the results obtained from  $n = 29$  cells using the protocol in A. An 88% increase in the mean oscillation frequency was detected after photoactivation of caged  $\text{IP}_3$ .

irradiation in the target cell and those adjacent to it). Finally, we evaluated the number of cells ( $N_{\text{cells}}$ ) in which  $[\text{Ca}^{2+}]_c$  reached an arbitrary threshold value (10% of the peak in the flashed cell). Model simulations replicated experimental responses (Fig. 5) with a number of gap junction channels  $N_{\text{ch}} = 935$  coupling each pair of neighboring cells (Fig. S5).

**Waves initiated by extracellular ATP puffs.** In cochlear organotypic cultures,  $\text{Ca}^{2+}$  waves can be triggered also by focal application of brief ATP puffs (4  $\mu\text{M}$ , 50 ms) from a glass micropipette placed in close proximity to a nonsensory cell (10, 11, 13, 19). We simulated these conditions by setting the model  $[\text{ATP}]_c$  initial value to 4  $\mu\text{M}$  in a focal spot of 2  $\mu\text{m}$  diameter for 50 ms and compared model responses to experimental results (Movie S1). Wave speed depends on both the maximal ATP release ( $v_{\text{HC}}$ ) and the ATP degradation rate ( $r_{\text{deg}}^{\text{ATP}}$ ). For  $300 \mu\text{M}\cdot\text{s}^{-1} \leq v_{\text{HC}} \leq 2,000 \mu\text{M}\cdot\text{s}^{-1}$  and low values of  $r_{\text{deg}}^{\text{ATP}}$  ( $< 0.1 \text{ s}^{-1}$ ), the model generated wave speeds in the range from 13  $\mu\text{m}\cdot\text{s}^{-1}$  to 17  $\mu\text{m}\cdot\text{s}^{-1}$  determined experimentally

(10, 11, 13, 19) (Fig. 6A). For  $r_{\text{deg}}^{\text{ATP}} > 0.1 \text{ s}^{-1}$ ,  $\text{Ca}^{2+}$  waves failed to propagate irrespective of the value attributed to  $v_{\text{HC}}$  in the above range because rapid degradation of the ATP released by any given cell hampered wave progression. Lowering  $v_{\text{HC}}$  (at constant  $r_{\text{deg}}^{\text{ATP}} < 0.1 \text{ s}^{-1}$ ) produced model responses, with progressively lower speed, which eventually lost their self-regenerative character (epitomized by a constant speed of propagation, Fig. 6B). At  $v_{\text{HC}} = 0$ ,  $\text{Ca}^{2+}$  signals invaded only first-order cells (Fig. 6B), consistent with experiments in which the extracellular purinergic pathway was abrogated pharmacologically by exposure to 200  $\mu\text{M}$  suramin (figure 4 of ref. 18). Note that, in agreement with experimental results, all traces in Fig. 6B superimpose for distances  $< 20 \mu\text{m}$  from the ATP source, as in this distance range cellular responses depend on direct activation by ATP diffusing out of the puff pipette. For some combinations of  $v_{\text{HC}}$  and  $r_{\text{deg}}^{\text{ATP}}$ , the model generated oscillatory  $\text{Ca}^{2+}$  waves (Fig. S6), which were occasionally observed in cochlear nonsensory cells (e.g., figure 9 of ref. 20).

Altogether, these data-driven simulations indicate that a self-regenerative ATP-induced ATP-release mechanism sustains wave propagation at constant speed over a vast range of distances (in excess of 200  $\mu\text{m}$  from the source). The transition from propagating to nonpropagating regimes is abrupt (Fig. 6A and C), indicating that (for each  $r_{\text{deg}}^{\text{ATP}}$  value) the system becomes self-regenerative only above a minimal threshold value of the  $v_{\text{HC}}$  parameter. At the opposite extreme, increasing  $v_{\text{HC}}$  results in propagation speeds that saturate at a value that depends on the ATP diffusion constant  $D$  in the extracellular medium (Fig. 6D), indicating that this parameter sets the ultimate limit to the cell-to-cell signal propagation (diffusion-limited rate).

Besides paracrine signaling mediated by extracellular ATP, our computational model also included  $\text{IP}_3$  diffusion between adjoining cells through gap junction channels (Fig. 1 and Supporting Information). However, the relative contribution to the propagation mechanism of gap junction channels (transferring  $\text{IP}_3$ ) and connexin hemichannels (releasing ATP) is unknown. Pharmacological isolation of the two components is difficult to achieve due to lack of connexin hemichannels blockers that do not also affect gap junction channels (29). Currently, hemichannel block without gap junction block is possible for connexin 43 (45) but not for connexin 26 and connexin 30. Computationally, gap junction

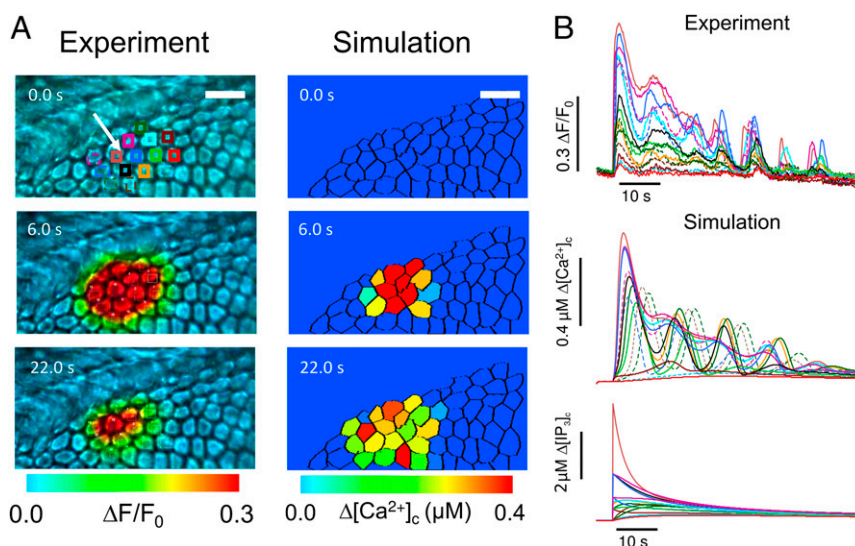


**Fig. 5.** Focal photoactivation of caged  $\text{IP}_3$ : comparison between experiments and simulations. (A) Cochlear cultures were loaded with the photoactivatable precursor of  $\text{IP}_3$ .  $[\text{Ca}^{2+}]_c$  oscillations and the propagation of  $\text{Ca}^{2+}$  signals between adjacent cells were elicited by illuminating a single cell, indicated by the white arrow, with a brief pulse of UV light (365 nm). Photolytic release of  $\text{IP}_3$  was reproduced in silico by a step increase of intracellular  $\text{IP}_3$  concentration. (Scale bar: 20  $\mu\text{m}$ .) (B) Time course of  $[\text{Ca}^{2+}]_c$  signals in experiments (Top) and simulations (Middle) from the regions of interest shown in A. The bottom set of traces is the corresponding model  $[\text{IP}_3]_c$  signals.

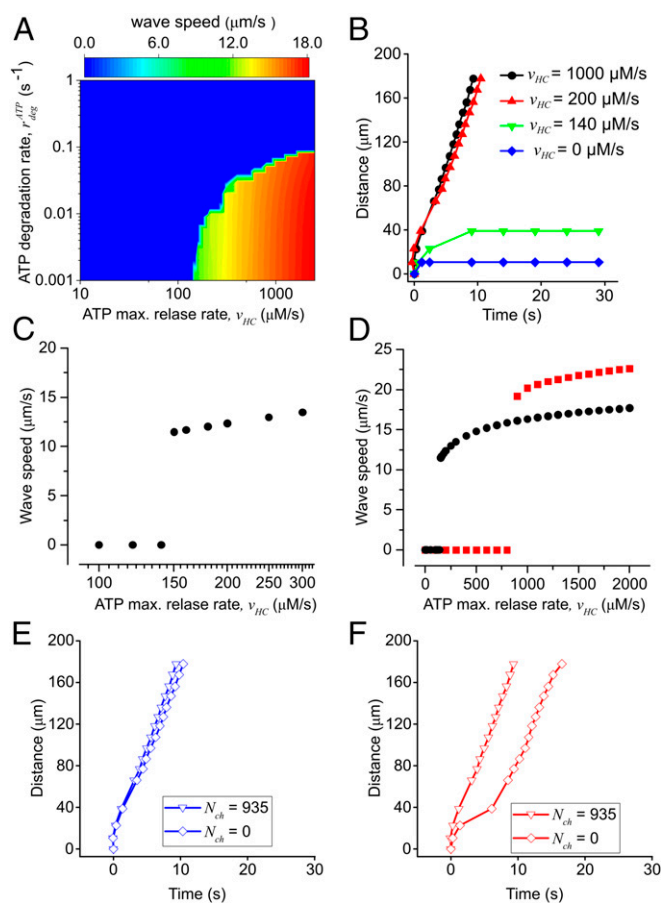


**Fig. 6.** Parametric analysis of radial  $\text{Ca}^{2+}$  wave propagation triggered by focal application of ATP. Experimental conditions were simulated by setting the model  $[\text{ATP}]_e$  initial value to  $4 \mu\text{M}$  in a focal spot of  $2 \mu\text{m}$  diameter for 50 ms. (A) Heat map showing the dependence of  $\text{Ca}^{2+}$  wave speed on the maximal ATP release rate,  $v_{\text{HC}}$ , and the ATP degradation constant,  $r_{\text{deg}}^{\text{ATP}}$ . Values in the blue region of the graph prevented ATP-induced  $\text{Ca}^{2+}$  wave propagation. (B) The maximal radius of the wave is plotted against time for different values of  $v_{\text{HC}}$  ( $0.0 \mu\text{M}\cdot\text{s}^{-1}$ ,  $140 \mu\text{M}\cdot\text{s}^{-1}$ ,  $200 \mu\text{M}\cdot\text{s}^{-1}$ , and  $1,000.0 \mu\text{M}\cdot\text{s}^{-1}$ ) at constant  $r_{\text{deg}}^{\text{ATP}} = 0.001 \text{ s}^{-1}$ . (C) Wave speed as a function of the ATP release rate  $v_{\text{HC}}$ , at constant  $r_{\text{deg}}^{\text{ATP}} = 0.001 \text{ s}^{-1}$ ; note discontinuity at  $v_{\text{HC}} = 150 \mu\text{M}\cdot\text{s}^{-1}$ , a value below which waves failed to propagate and above which waves propagate with speed  $> 11 \mu\text{m}\cdot\text{s}^{-1}$ . (D) The same as C, but with values plotted on a larger, linear scale; for large values of  $v_{\text{HC}}$ , wave speed saturates to an asymptotic value that depends on the ATP diffusion coefficient  $D$ : black circles,  $D = 363 \mu\text{m}^2\cdot\text{s}^{-1}$  (correct value); red squares,  $D = 726 \mu\text{m}^2\cdot\text{s}^{-1}$  (hypothetical value, to make the point). Note that also the value of  $v_{\text{HC}}$  at which the discontinuity arises depends on the diffusion coefficient  $D$ , as higher values cause faster diffusion of ATP away from the endolymphatic surface of the cells, and thus more ATP release is required to generate  $\text{Ca}^{2+}$  waves. (E and F)  $\text{Ca}^{2+}$  wave radius vs. time for  $v_{\text{HC}} = 1,000.0 \mu\text{M}\cdot\text{s}^{-1}$  and  $r_{\text{deg}}^{\text{ATP}} = 0.01 \text{ s}^{-1}$  in the presence (triangles) or absence (squares) of gap-junction-mediated  $\text{IP}_3$  diffusion. The fraction of ATP-releasing supporting cells is 100% in E and 50% in F. Data points for  $N_{\text{ch}} = 935$  are the same in E and F.

channels blockade can be simulated by setting  $N_{\text{ch}} = 0$  while leaving all other parameters unchanged (and thus also hemichannel function). When all model cells were allowed to release ATP, abrogation of gap junction coupling resulted in negligible changes to the  $\text{Ca}^{2+}$  wave speed (Fig. 6E). The contribution of  $\text{IP}_3$  diffusion through gap junction channels became appreciable only upon reducing the number of model cells that were allowed to release ATP (Fig. 6F). Therefore, our computational results single out ATP-induced ATP release through connexin hemichannels as the primary mechanism responsible for long-range propagation of  $\text{Ca}^{2+}$  signals in the developing mouse cochlea.

## Discussion

The results of the assay we performed based on ref. 32 confirm that  $[\text{IP}_3]_e$  oscillations are not an obligatory component of  $[\text{Ca}^{2+}]_e$  oscillations (30–32) in cochlear nonsensory cells. Accordingly, we constructed a computational model for the occurrence of  $[\text{Ca}^{2+}]_e$  oscillations based on sequential positive and negative feedback of  $\text{Ca}^{2+}$  on the  $\text{IP}_3$  receptor. As has been previously described in models of this type (32),  $\text{Ca}^{2+}$  oscillations also may develop at constant  $[\text{IP}_3]_e$ . Of note, our model (i) captures the range of values of  $[\text{ATP}]_e$  that evoke  $[\text{Ca}^{2+}]_e$  oscillations in nonsensory cells, (ii) accounts for the dose–response relationship between  $[\text{Ca}^{2+}]_e$  and  $[\text{ATP}]_e$ , and (iii) links the occurrence of  $[\text{Ca}^{2+}]_e$  oscillations in a well-defined range of  $[\text{ATP}]_e$  to supercritical Hopf bifurcations (34).

The model highlights also another critical behavior, namely the abrupt (discontinuous) transition from propagating regimes (intercellular  $\text{Ca}^{2+}$  wave speed  $> 11 \mu\text{m}\cdot\text{s}^{-1}$ ) to propagation failure (speed = 0) that occurs upon lowering the maximal ATP release rate ( $v_{\text{HC}}$  parameter, Table S1) below a minimal threshold value, which depends on ATP degradation rate ( $r_{\text{deg}}^{\text{ATP}}$  parameter, Table S1). Previous experiments with ATP biosensor cells demonstrated that photostimulation with caged  $\text{IP}_3$  releases ATP to the extracellular medium at the endolymphatic surface of the lesser epithelial ridge and triggers intercellular  $\text{Ca}^{2+}$  wave propagation (19). Similar waves were also evoked by photostimulation with caged  $\text{IP}_3$  in the greater epithelial ridge (13). Leybaert and coworkers showed that (i) an  $\text{IP}_3$ -mediated increase in the  $[\text{Ca}^{2+}]_e$  is sufficient to trigger hemichannel opening and (ii) hemichannel open probability has a bell-shaped relationship with  $[\text{Ca}^{2+}]_e$  (21–23). The hemichannel scheme in our model, although oversimplified, captures these critically important experimental results. However, a bell-shaped dependence on  $[\text{Ca}^{2+}]_e$  has been demonstrated for connexins 32 and 43 (21–23). Whether this applies also to connexins 26 and 30, although very likely, awaits direct experimental confirmation. Provided sufficient ATP is released through connexin hemichannels, its binding to  $\text{P}_2\text{Y}$  receptors (10, 11) activates PLC-dependent  $\text{IP}_3$  production in a population of nearby cells (13). This in turn promotes  $\text{Ca}^{2+}$  release from intracellular stores, raising  $[\text{Ca}^{2+}]_e$ , which, up to  $\sim 500 \text{ nM}$ , increases the hemichannel open probability (21–23), fostering further ATP-dependent ATP release in a self-regenerative cascade of biochemical reactions that sustains  $\text{Ca}^{2+}$  wave propagation at constant speed across the cell network.

It is important to note that the four parameters of our simplified hemichannel model would still fit the experimental data if they were all scaled by the same value, thus making the opening kinetics faster or slower. With the particular set of parameters we used, the hemichannel open probability peaks in  $\sim 200 \text{ ms}$  following a steplike increase of the  $[\text{Ca}^{2+}]_e$ , which seems reasonable given that the effect of intracellular  $\text{Ca}^{2+}$  on hemichannel gating is likely an indirect one (23). A slower response seems unlikely, and faster kinetics would not affect much the propagation speed of  $\text{Ca}^{2+}$  waves, because  $\text{IP}_3$  production and  $\text{Ca}^{2+}$  release are the rate-limiting factors in this process.

We also ran some simulations using a two-state hemichannel model (open and closed states) in which hemichannel inactivation at high  $\text{Ca}^{2+}$  is not present (Fig. S7). The results we obtained for the ATP-evoked propagation of  $\text{Ca}^{2+}$  waves resemble those generated by the four-state model. Thus, inactivation by high  $\text{Ca}^{2+}$  is not required for the propagation of  $\text{Ca}^{2+}$  waves and for the associated ATP-induced ATP release. We expect that similar results can be obtained with other types of hemichannel models (e.g., a three-state model, with an open, a closed, and an inactive state) as long as the open probability is different from 0 at physiological  $\text{Ca}^{2+}$  levels. For all these reasons, we believe that our conclusions are robust and independent of the particular hemichannel models or kinetics.

We have previously implicated  $\text{IP}_3$  synthesis deficits (13) as well as gap junction channel  $\text{IP}_3$  permeability defects (18) in the

pathogenesis of hereditary hearing disorders. Furthermore, using a knock-in mouse model, we have linked defects in the spontaneous release of ATP from connexin hemichannels in the developing cochlea to disease phenotype in adulthood (28). The unitary permeability of gap junction channels to  $\text{IP}_3$  ( $p_u$ , Table S1) is an important parameter in our numerical simulations of  $\text{IP}_3$ -evoked intercellular  $\text{Ca}^{2+}$  waves. It has been proposed that junctions in the murine cochlea are composed of connexin 26/30 heteromeric connexons (14, 15), although this may not be the case for the human cochlea (46). As the  $p_u$  of heterotypic/heteromeric channels is not known, we used the value we previously determined for homomeric/homotypic connexin 26 channels in transfected HeLa cells (44). Another critical model parameter that influences cell coupling is the average number of channels ( $N_{\text{ch}}$ ) shared by each cell pair in the syncytium. Using voltage imaging, we previously estimated that nonsensory cells in the apical coil of the cochlea are coupled by 910–1,260 open channels per cell pair (47). This range of values is compatible with the estimate of  $N_{\text{ch}} = 935$  obtained here, by a completely different approach, to account for the propagation range of  $\text{Ca}^{2+}$  signals evoked by photolytic release of  $\text{IP}_3$ .

Estimating the number of open hemichannels that release ATP is more difficult than estimating the number of gap junction channels between supporting cells, mainly because the unitary permeability of hemichannels to ATP is not known; we provide an educated guess in *Supporting Information*. In the light of the present analysis, ATP release through connexin hemichannels of the cochlear sensory epithelium, and subsequent diffusion through endolymph (19), appears to influence intercellular  $\text{Ca}^{2+}$  signaling more drastically than the cell-to-cell diffusion of  $\text{IP}_3$  through gap junction channels (18). On the other hand, permeation of these two signaling molecules, which are both highly negatively charged and have similar size (Movie S2), is most likely correlated (48). Therefore, a point mutation that affects  $\text{IP}_3$  passage through the channel pore may affect also the passage of ATP and vice versa.

The propagation of ATP-dependent intercellular  $\text{Ca}^{2+}$  waves has been described in glial cells (which express connexins 40, 43, 45, and 46) (49) as well as in a variety of other connexin-expressing epithelial tissues, including (but not limited to) airway epithelia (connexin 32) (50), vascular endothelium (connexins 37, 40, 43, and 45) (51), keratinocytes (connexins 26, 30, 30.3, 31.1, 37, and 43) (52), renal glomerular endothelial cells (connexin 40) (53), and corneal endothelial cells (connexin 43) (54). We believe that the combination of experimental measurements and computational modeling presented here is of general interest as it (*i*) overcomes major limitations due to lack of specific connexin channel inhibitors and (*ii*) can be readily extended (by suitable changes to the set of parameters in Table S1) to other cellular systems, including (but not limited to) those mentioned above.

Finally, the results of this modeling offer critical insight into the unique operating conditions of connexin hemichannels at the endolymphatic surface of the cochlear sensory epithelium. All hemichannels are activated upon depolarization and are effectively closed by hyperpolarization; however, voltage dependence, kinetic properties, and sensitivity to  $[\text{Ca}^{2+}]_o$ , which acts as an open pore blocker (55), vary significantly between hemichannels composed of different connexin isoforms (56). At transmembrane potentials ( $\Delta V_m$ , inside minus outside)  $\leq -30$  mV, connexin 30 hemichannels have zero open probability also in zero  $[\text{Ca}^{2+}]_o$  (57). Under the same conditions, connexin 26 hemichannels transit frequently between open and closed states (58, 59). This peculiar behavior has been attributed to the so-called “loop gate,” which remains constitutively active at all voltages even in zero  $[\text{Ca}^{2+}]_o$  (58). The same behavior is not observed in hemichannels formed by other connexins (e.g., connexins 46 and 50), which remain stably open in low  $[\text{Ca}^{2+}]_o$  and close only if subjected to robust hyperpolarization (60, 61).

Depolarization promotes hemichannel opening, and therefore the cell resting potential (and input resistance of the plasma membrane) can be completely run down in the presence of strong hemichannel activity (56). However, the resting potential of nonsensory cells in cochlear organotypic cultures exposed to endolymph-like  $[\text{Ca}^{2+}]_o$  (20  $\mu\text{M}$ ) is  $\leq -60$  mV (47). We conclude that, at resting  $[\text{Ca}^{2+}]_c$  and in 20  $\mu\text{M}$   $[\text{Ca}^{2+}]_o$ , hemichannels of nonsensory cells of the lesser epithelial ridge are only modestly active and transient hemichannel opening promotes ATP release that is constantly neutralized by the action of ectonucleotidases.

Consistent with this conclusion, nonsensory cells of the lesser epithelial ridge remain quiescent if not perturbed by stimuli (e.g., extracellular ATP or intracellular  $\text{IP}_3$ ) that promote hemichannel opening by elevating the  $[\text{Ca}^{2+}]_c$ . However, they develop spontaneous  $\text{Ca}^{2+}$  oscillations when exposed to an ectonucleotidase inhibitor, such as ARL67156 (19). As already mentioned, the same PLC- and  $\text{IP}_3\text{R}$ -dependent signal transduction cascade activated by extracellular ATP governs  $[\text{Ca}^{2+}]_c$  oscillations and  $\text{Ca}^{2+}$  waves in cochlear nonsensory cells of the greater epithelial ridge (13). Therefore, the occurrence of ATP-dependent spontaneous  $\text{Ca}^{2+}$  signaling activity in the greater epithelial ridge (13, 27, 28) is likely due to a constitutively lower ectonucleotidase activity at the endolymphatic surface of the tall columnar cells that populate that portion of the developing sensory epithelium.

In vivo, the  $\Delta V_m$  across the apical plasma membrane of all cells exposed to endolymph depends on the series combination of the cell resting potential and the endocochlear potential (1). In mice, the endocochlear potential remains below 15 mV between P1 and P5 and increases rapidly after P7, reaching levels of 80–100 mV around P16 (38). In adult mice, we measured endocochlear potentials as large as 117 mV (62). In adult nonsensory cells of the rodent organ of Corti, the cell resting potential can be as negative as  $-90$  mV (63); therefore the  $\Delta V_m$  across their apical plasma membrane can exceed  $-200$  mV (inside minus outside). Extrapolating available data, which cover a range from  $+60$  mV to  $-100$  mV (57, 59), suggests that a  $\Delta V_m$  around  $-200$  mV should be more than enough to keep connexin 26 (and certainly connexin 30) hemichannels closed in endolymphatic  $[\text{Ca}^{2+}]_o$ . Hemichannel opening may still occur under conditions that promote a reduction of the  $\Delta V_m$  (64). Acting synergistically with ATP-gated ion channels (7, 8), the release of ATP into endolymph through connexin hemichannels of the adult cochlea may then foster adaptation to elevated sound levels.

## Materials and Methods

**Mathematical Methods and Model Parameters.** A schematic representation of the model is shown in Fig. 1. The model comprises three main subsystems ( $\text{Ca}^{2+}$ ,  $\text{IP}_3$ , and ATP) as described in detail in *Supporting Information*. Model parameters are summarized in Table S1.

**Preparation of Cochlear Organotypic Cultures.** Animal work was approved by the Ethics committee of the University of Padua (Comitato Etico di Ateneo per la Sperimentazione Animale, protocol no. 104230, October 12, 2013). Cochleae were dissected from P5 mouse pups in ice-cold Hepes-buffered (10 mM, pH 7.2) HBSS, placed onto glass coverslips coated with 185  $\mu\text{g}/\text{mL}$  of Cell Tak, and incubated overnight at 37 °C in DMEM/F12 supplemented with 5% (vol/vol) FBS.

**Ratiometric  $\text{Ca}^{2+}$  Imaging.** In this study, we used membrane-permeable AM ester derivatives of Fura-2 (Thermo Fisher Scientific, catalog no. F1221), Fluo-4 (Thermo Fisher Scientific, catalog no. F14217), and caged inositol (3,4,5) trisphosphate [iso-Ins(1,4,5)P3/PM caged, Enzo Life Sciences, catalog no. ALX307071]. Pluronic F-127 (catalog no. P2443) and sulphinyprazole (catalog no. S9509) were purchased from Sigma-Aldrich. All experiments were performed at room temperature (22–25 °C). Cochlear cultures were transferred to the stage of an upright wide-field fluorescence microscope (BX51; Olympus) and continually superfused with EXM, an extracellular medium containing 138 mM NaCl, 5 mM KCl, 2 mM  $\text{CaCl}_2$ , 0.3 mM  $\text{NaH}_2\text{PO}_4$ , 0.4 mM  $\text{KH}_2\text{PO}_4$ , 10 mM Hepes-NaOH, and 6 mM d-glucose (pH 7.2, 300 mOsm). Cochlear cultures were incubated for 40 min at 37 °C in DMEM supplemented

with Fura-2 AM (16  $\mu\text{M}$ ). The incubation medium contained also pluronic F-127 (0.1%, wt/vol) and sulfinpyrazone (250  $\mu\text{M}$ ) to prevent dye sequestration and secretion. Cultures were then transferred onto the stage of an upright microscope (BX51; Olympus) and perfused in EXM for 20 min at 2 mL/min to allow for deesterification. For recording, EXM was substituted by ECM, a medium obtained by replacing 2 mM  $\text{Ca}^{2+}$  in EXM with an endolymph-like concentration (20  $\mu\text{M}$ ). Fura-2 fluorescence was excited using alternatively two light-emitting diodes (LEDs) (center wavelengths 365 nm and 385 nm; M365L and M385L, Thorlabs) passing through an FF01-360/12-2 and an FF01-387-11 filter, respectively (Semrock), and directed onto the sample through a dichromatic mirror (T400LP; Chroma). Fluorescence emission was selected by a BA495-540HQ filter (Olympus) to form fluorescence images on a scientific-grade CCD camera (SensiCam, PCO AG), using a 60 $\times$  water immersion objective (N.A. 1.0, Fluor; Nikon). Image sequences were acquired using software developed in the laboratory, stored on a disk, and processed offline using the Matlab software package (The MathWorks). Signals were measured as dye emission ratio changes,  $\Delta R = R(t) - R(0)$ , where  $t$  is time and  $R(t)$  is emission intensity excited at 365 nm divided by the intensity excited at 385 nm, and  $R(0)$  indicates prestimulus ratio. To directly compare fluorescence measurements to  $\text{Ca}^{2+}$  concentrations computed with computer simulations, we converted fluorescence intensity ratios  $R$  to  $[\text{Ca}^{2+}]_c$  values by the Grynkiewicz equation (65)

$$[\text{Ca}^{2+}]_c = K_D \frac{R - R_{\min}}{R_{\max} - R} \frac{F_{\max}}{F_{\min}}$$

where  $K_D = 287.3$  nM is the Fura-2 dissociation constant at 25  $^{\circ}\text{C}$  (66);  $R_{\min}$  and  $R_{\max}$  are ratio values in  $\text{Ca}^{2+}$ -free conditions and in saturating  $\text{Ca}^{2+}$  conditions, respectively; and  $F_{\min}/F_{\max}$  is the ratio of the fluorescence intensity after excitation at 385 nm in free and saturating  $\text{Ca}^{2+}$  conditions, respectively.

$R_{\max}$  and  $F_{\max}$  were measured by perfusing cochlear cultures with an extracellular solution containing 10  $\mu\text{M}$  ionomycin and 5 mM  $\text{Ca}^{2+}$  for 2 min.  $R_{\min}$  and  $F_{\min}$  were measured after perfusion with a solution containing 100  $\mu\text{M}$  EGTA and 10  $\mu\text{M}$  ionomycin for 30 min. The overall  $[\text{Ca}^{2+}]_c$  of the cell was computed by averaging  $R$  values in a region of interest centered on it.

For ATP stimulation experiments, ATP dissolved in ECM was applied by pressure, using glass microcapillaries (puff pipettes) that were pulled to a tip of 2–10  $\mu\text{m}$  on a vertical puller (PP80; Narishige) and placed near the target cell. Pressure was applied at the back of the pipette by delivering a transistor–transistor logic (TTL) pulse of carefully controlled duration to a Pneumatic PicoPump (PV800; World Precision Instruments) under software control. All cells tested responded to ATP, whereas no response was detected when ATP (or other P2YR agonists) was omitted from the solution used to fill the puff pipette, indicating that accidental mechanical activation of the cells was negligible.

**Photostimulation with Caged  $\text{IP}_3$ .** Cochlear cultures were incubated for 30 min at 37  $^{\circ}\text{C}$  in DMEM supplemented with the  $\text{Ca}^{2+}$  dye Fluo-4 AM (16  $\mu\text{M}$ ), caged  $\text{IP}_3$  AM (5  $\mu\text{M}$ ), pluronic F-127 (0.1%, wt/vol), and sulfinpyrazone (250  $\mu\text{M}$ ) and thereafter perfused in EXM for 10 min at 2 mL/min to allow for deesterification. Fluorescence emission was selected by an ET535/30M filter (Chroma), centered around a 535-nm wavelength, to form fluorescence images on a scientific-grade CCD camera (SensiCam; PCO AG) using a 20 $\times$  water immersion objective (N.A. 0.95, LumPlanFI; Olympus) connected to a microscope (BX51; Olympus) and illuminated by a collimated 470-nm light-emitting diode (M470L2; Thorlabs) directed onto the sample through a dichromatic mirror (505 dcm; Chroma). For focal photostimulation with caged  $\text{IP}_3$ , the output of a TTL-controlled semiconductor laser module (20 mW, 379 nm, part no. FBB-375-020-FS-FS-1-1; RGBLase LLC) was injected into a UV-permissive fiber-optic cable (multimode step index 0.22 N.A., 105- $\mu\text{m}$  core, part no. AFS105/125YCUSTOM; Thorlabs GmbH). Fiber output was projected onto the specimen plane by an aspheric condenser lens (20-mm effective focal length, part no. ACL2520; Thorlabs) and the recollimated beam was directed onto a dichromatic mirror (400 dclp; Chroma) placed at 45 $^{\circ}$  just above the objective lens of the microscope. By carefully adjusting the position of the fiber in front of the aspheric lens we projected a sharp image of the illuminated fiber core (spot) onto the specimen focal plane selected by the (infinity-corrected) objective lens. Under these conditions, the fiber-optic diameter determined accurately the laser-irradiated area. The size of the irradiated area was estimated by measuring the dimensions of the spot carved by the focused laser into a thin film of black ink deposited on a microscope coverslip located at the front focal plane of the objective. On average, this area comprised a central cell and its six nearest neighbors ( $\text{Ca}^{2+}$  signal generators). Baseline (prestimulus) fluorescence emission ( $F_0$ ) was recorded for 2 s, and thereafter a UV laser pulse of 170 ms was applied to release  $\text{IP}_3$  and fluorescence emission was monitored for up to 60 s. Signals were measured as relative changes of fluorescence emission intensity ( $\Delta F/F_0$ ), where  $F$  is fluorescence at poststimulus time  $t$  and  $\Delta F = F - F_0$ .

**Statistical Analysis.** Means are quoted  $\pm$  SEM and  $P$  values are indicated by the letter  $P$ . Statistical comparisons were made using the Mann–Whitney  $U$  test and  $P < 0.05$  was selected as the criterion for statistical significance.

**ACKNOWLEDGMENTS.** We thank Francesco Zonta for providing [Movie S2](#) and Giulia Crispino for immunofluorescence staining and laser scanning confocal imaging of fixed cochlear organotypic cultures ([Fig. S1](#)). This work was supported by Fondazione Telethon (Grant GGP13114 to F.M.), the Italian National Research Council (Project DSB.AD009.001.004/INVECCHIAMENTO IBCN to F.M.) and the Italian Ministry of University and Research (Grant FIRB-RBAP11X42L to T.P.). F.C. was supported by a junior postdoctoral fellowship from the University of Padua (Grant CPDR132235 to F.M.).

- Fettiplace R, Kim KX (2014) The physiology of mechano-electrical transduction channels in hearing. *Physiol Rev* 94(3):951–986.
- Mammano F (2013) ATP-dependent intercellular  $\text{Ca}^{2+}$  signaling in the developing cochlea: Facts, fantasies and perspectives. *Semin Cell Dev Biol* 24(1):31–39.
- Lim D, Rueda J (1992) Structural development of the cochlea. *Development of Auditory and Vestibular Systems - 2*, ed Romand R (Elsevier, New York), 1st Ed, pp 33–58.
- Eggston AA, Wolff D (1947) Embryology of the ear. *Histopathology of the Ear, Nose, and Throat* (Williams and Wilkins, Baltimore), pp 37–64.
- Rio C, Dikkes P, Liberman MC, Corfas G (2002) Glial fibrillary acidic protein expression and promoter activity in the inner ear of developing and adult mice. *J Comp Neurol* 442(2):156–162.
- Housley GD, Bringmann A, Reichenbach A (2009) Purinergic signaling in special senses. *Trends Neurosci* 32(3):128–141.
- Housley GD, et al. (2013) ATP-gated ion channels mediate adaptation to elevated sound levels. *Proc Natl Acad Sci USA* 110(18):7494–7499.
- Yan D, et al. (2013) Mutation of the ATP-gated P2X(2) receptor leads to progressive hearing loss and increased susceptibility to noise. *Proc Natl Acad Sci USA* 110(6):2228–2233.
- Kikuchi T, Kimura RS, Paul DL, Takasaka T, Adams JC (2000) Gap junction systems in the mammalian cochlea. *Brain Res Brain Res Rev* 32(1):163–166.
- Gale JE, Piazza V, Ciubotaru CD, Mammano F (2004) A mechanism for sensing noise damage in the inner ear. *Curr Biol* 14(6):526–529.
- Piazza V, Ciubotaru CD, Gale JE, Mammano F (2007) Purinergic signalling and intercellular  $\text{Ca}^{2+}$  wave propagation in the organ of Corti. *Cell Calcium* 41(1):77–86.
- Berridge MJ (2009) Inositol trisphosphate and calcium signalling mechanisms. *Biochim Biophys Acta* 1793(6):933–940.
- Rodriguez L, et al. (2012) Reduced phosphatidylinositol 4,5-bisphosphate synthesis impairs inner ear  $\text{Ca}^{2+}$  signaling and high-frequency hearing acquisition. *Proc Natl Acad Sci USA* 109(35):14013–14018.
- Forge A, et al. (2003) Gap junctions in the inner ear: Comparison of distribution patterns in different vertebrates and assessment of connexin composition in mammals. *J Comp Neurol* 467(2):207–231.
- Ahmad S, Chen S, Sun J, Lin X (2003) Connexins 26 and 30 are co-assembled to form gap junctions in the cochlea of mice. *Biochem Biophys Res Commun* 307(2):362–368.
- Ortolano S, et al. (2008) Coordinated control of connexin 26 and connexin 30 at the regulatory and functional level in the inner ear. *Proc Natl Acad Sci USA* 105(48):18776–18781.
- Zonta F, Polles G, Zanotti G, Mammano F (2012) Permeation pathway of homomeric connexin 26 and connexin 30 channels investigated by molecular dynamics. *J Biomol Struct Dyn* 29(5):985–998.
- Beltramello M, Piazza V, Bukauskas FF, Pozzan T, Mammano F (2005) Impaired permeability to  $\text{Ins}(1,4,5)\text{P}_3$  in a mutant connexin underlies recessive hereditary deafness. *Nat Cell Biol* 7(1):63–69.
- Anselmi F, et al. (2008) ATP release through connexin hemichannels and gap junction transfer of second messengers propagate  $\text{Ca}^{2+}$  signals across the inner ear. *Proc Natl Acad Sci USA* 105(48):18770–18775.
- Majumder P, et al. (2010) ATP-mediated cell-cell signaling in the organ of Corti: The role of connexin channels. *Purinergic Signal* 6(2):167–187.
- Leybaert L, et al. (2003) Connexin channels, connexin mimetic peptides and ATP release. *Cell Commun Adhes* 10(4-6):251–257.
- De Vuyst E, et al. (2006) Intracellular calcium changes trigger connexin 32 hemichannel opening. *EMBO J* 25(1):34–44.
- De Vuyst E, et al. (2009)  $\text{Ca}^{2+}$  regulation of connexin 43 hemichannels in C6 glioma and glial cells. *Cell Calcium* 46(3):176–187.
- Uhlén P, Fritsch N (2010) Biochemistry of calcium oscillations. *Biochem Biophys Res Commun* 396(1):28–32.
- Parekh AB (2011) Decoding cytosolic  $\text{Ca}^{2+}$  oscillations. *Trends Biochem Sci* 36(2):78–87.
- Leybaert L, Sanderson MJ (2012) Intercellular  $\text{Ca}^{2+}$  waves: Mechanisms and function. *Physiol Rev* 92(3):1359–1392.
- Fritsch NX, Yi E, Gale JE, Glowatzki E, Bergles DE (2007) The origin of spontaneous activity in the developing auditory system. *Nature* 450(7166):50–55.
- Schütt M, et al. (2010) The human deafness-associated connexin 30 T5M mutation causes mild hearing loss and reduces biochemical coupling among cochlear non-sensory cells in knock-in mice. *Hum Mol Genet* 19(24):4759–4773.

29. Sáez JC, Leybaert L (2014) Hunting for connexin hemichannels. *FEBS Lett* 588(8):1205–1211.
30. Li W, Llopis J, Whitney M, Zlokarnik G, Tsien RY (1998) Cell-permeant caged InsP3 ester shows that Ca<sup>2+</sup> spike frequency can optimize gene expression. *Nature* 392(6679):936–941.
31. Matsu-ura T, et al. (2006) Cytosolic inositol 1,4,5-trisphosphate dynamics during intracellular calcium oscillations in living cells. *J Cell Biol* 173(5):755–765.
32. Sneyd J, et al. (2006) A method for determining the dependence of calcium oscillations on inositol trisphosphate oscillations. *Proc Natl Acad Sci USA* 103(6):1675–1680.
33. Gaspers LD, et al. (2014) Hormone-induced calcium oscillations depend on cross-coupling with inositol 1,4,5-trisphosphate oscillations. *Cell Reports* 9(4):1209–1218.
34. Strogatz SH (2001) *Nonlinear Dynamics and Chaos* (Westview, Boulder, CO).
35. Nin F, et al. (2008) The endocochlear potential depends on two K(+) diffusion potentials and an electrical barrier in the stria vascularis of the inner ear. *Proc Natl Acad Sci USA* 105(5):1751–1756.
36. Anniko M, Wróblewski R (1986) Ionic environment of cochlear hair cells. *Hear Res* 22:279–293.
37. Boshier SK, Warren RL (1978) Very low calcium content of cochlear endolymph, an extracellular fluid. *Nature* 273(5661):377–378.
38. Yamasaki M, Komune S, Shimozono M, Matsuda K, Haruta A (2000) Development of monovalent ions in the endolymph in mouse cochlea. *ORL J Otorhinolaryngol Relat Spec* 62(5):241–246.
39. Wong AC, Birnbaumer L, Housley GD (2013) Canonical transient receptor potential channel subtype 3-mediated hair cell Ca(2+) entry regulates sound transduction and auditory neurotransmission. *Eur J Neurosci* 37(9):1478–1486.
40. Erb L, Weisman GA (2012) Coupling of P2Y receptors to G proteins and other signaling pathways. *Wiley Interdiscip Rev Membr Transp Signal* 1(6):789–803.
41. Arnol'd VI (1994) *Bifurcation Theory and Catastrophe Theory* (Springer, Berlin).
42. Bezprozvanny I, Watras J, Ehrlich BE (1991) Bell-shaped calcium-response curves of Ins(1,4,5)P<sub>3</sub>- and calcium-gated channels from endoplasmic reticulum of cerebellum. *Nature* 351(6329):751–754.
43. Adkins CE, Taylor CW (1999) Lateral inhibition of inositol 1,4,5-trisphosphate receptors by cytosolic Ca(2+). *Curr Biol* 9(19):1115–1118.
44. Hernandez VH, et al. (2007) Unitary permeability of gap junction channels to second messengers measured by FRET microscopy. *Nat Methods* 4(4):353–358.
45. Wang N, et al. (2013) Selective inhibition of Cx43 hemichannels by Gap19 and its impact on myocardial ischemia/reperfusion injury. *Basic Res Cardiol* 108(1):309.
46. Liu W, et al. (2016) Super-resolution structured illumination fluorescence microscopy of the lateral wall of the cochlea: The Connexin26/30 proteins are separately expressed in man. *Cell Tissue Res* 365(1):13–27.
47. Ceriani F, Mammano F (2013) A rapid and sensitive assay of intercellular coupling by voltage imaging of gap junction networks. *Cell Commun Signal* 11:78.
48. Harris AL (2007) Connexin channel permeability to cytoplasmic molecules. *Prog Biophys Mol Biol* 94(1-2):120–143.
49. Guthrie PB, et al. (1999) ATP released from astrocytes mediates glial calcium waves. *J Neurosci* 19(2):520–528.
50. Isakson BE, Evans WH, Boitano S (2001) Intercellular Ca<sup>2+</sup> signaling in alveolar epithelial cells through gap junctions and by extracellular ATP. *Am J Physiol Lung Cell Mol Physiol* 280(2):L221–L228.
51. Lohman AV, Billaud M, Isakson BE (2012) Mechanisms of ATP release and signalling in the blood vessel wall. *Cardiovasc Res* 95(3):269–280.
52. Tsutsumi M, Denda S, Inoue K, Ikeyama K, Denda M (2009) Calcium ion gradients and dynamics in cultured skin slices of rat hindpaw in response to stimulation with ATP. *J Invest Dermatol* 129(3):584–589.
53. Toma I, et al. (2008) Connexin 40 and ATP-dependent intercellular calcium wave in renal glomerular endothelial cells. *Am J Physiol Regul Integr Comp Physiol* 294(6):R1769–R1776.
54. Gomes P, Srinivas SP, Vereecke J, Himpens B (2005) ATP-dependent paracrine intercellular communication in cultured bovine corneal endothelial cells. *Invest Ophthalmol Vis Sci* 46(1):104–113.
55. Bennett BC, et al. (2016) An electrostatic mechanism for Ca(2+)-mediated regulation of gap junction channels. *Nat Commun* 7:8770.
56. Fasciani I, et al. (2013) Regulation of connexin hemichannel activity by membrane potential and the extracellular calcium in health and disease. *Neuropharmacology* 75:479–490.
57. Valiunas V, Weingart R (2000) Electrical properties of gap junction hemichannels identified in transfected HeLa cells. *Pflügers Arch* 440(3):366–379.
58. Sanchez HA, Slavi N, Srinivas M, Verselis VK (2016) Syndromic deafness mutations at Asn 14 differentially alter the open stability of Cx26 hemichannels. *J Gen Physiol* 148(1):25–42.
59. Sanchez HA, Villone K, Srinivas M, Verselis VK (2013) The D50N mutation and syndromic deafness: Altered Cx26 hemichannel properties caused by effects on the pore and intersubunit interactions. *J Gen Physiol* 142(1):3–22.
60. Trexler EB, Bennett MV, Bargiello TA, Verselis VK (1996) Voltage gating and permeation in a gap junction hemichannel. *Proc Natl Acad Sci USA* 93(12):5836–5841.
61. Srinivas M, Kronengold J, Bukauskas FF, Bargiello TA, Verselis VK (2005) Correlative studies of gating in Cx46 and Cx50 hemichannels and gap junction channels. *Biophys J* 88(3):1725–1739.
62. Crispino G, et al. (2011) BAAV mediated GJB2 gene transfer restores gap junction coupling in cochlear organotypic cultures from deaf Cx26<sup>50x10</sup>Cre mice. *PLoS One* 6(8):e23279.
63. Oesterle EC, Dallos P (1990) Intracellular recordings from supporting cells in the guinea pig cochlea: DC potentials. *J Neurophysiol* 64(2):617–636.
64. Thorne PR, Muñoz DJ, Housley GD (2004) Purinergic modulation of cochlear partition resistance and its effect on the endocochlear potential in the Guinea pig. *J Assoc Res Otolaryngol* 5(1):58–65.
65. Gryniewicz G, Poenie M, Tsien RY (1985) A new generation of Ca<sup>2+</sup> indicators with greatly improved fluorescence properties. *J Biol Chem* 260(6):3440–3450.
66. Larsson D, Larsson B, Lundgren T, Sundell K (1999) The effect of pH and temperature on the dissociation constant for fura-2 and their effects on [Ca(2+)]<sub>i</sub> in enterocytes from a poikilothermic animal, Atlantic cod (*Gadus morhua*). *Anal Biochem* 273(1):60–65.
67. De Young GW, Keizer J (1992) A single-pool inositol 1,4,5-trisphosphate-receptor-based model for agonist-stimulated oscillations in Ca<sup>2+</sup> concentration. *Proc Natl Acad Sci USA* 89(20):9895–9899.
68. De Pittà M, Goldberg M, Volman V, Berry H, Ben-Jacob E (2009) Glutamate regulation of calcium and IP<sub>3</sub> oscillating and pulsating dynamics in astrocytes. *J Biol Phys* 35(4):383–411.
69. Agulhon C, et al. (2008) What is the role of astrocyte calcium in neurophysiology? *Neuron* 59(6):932–946.
70. Lytton J, Westlin M, Burk SE, Shull GE, MacLennan DH (1992) Functional comparisons between isoforms of the sarcoplasmic or endoplasmic reticulum family of calcium pumps. *J Biol Chem* 267(20):14483–14489.
71. Li YX, Rinzel J (1994) Equations for InsP<sub>3</sub> receptor-mediated [Ca<sup>2+</sup>]<sub>i</sub> oscillations derived from a detailed kinetic model: A Hodgkin-Huxley like formalism. *J Theor Biol* 166(4):461–473.
72. Lemon G, Gibson WG, Bennett MR (2003) Metabotropic receptor activation, desensitization and sequestration-I: Modelling calcium and inositol 1,4,5-trisphosphate dynamics following receptor activation. *J Theor Biol* 223(1):93–111.
73. Sneyd J, Wetton BT, Charles AC, Sanderson MJ (1995) Intercellular calcium waves mediated by diffusion of inositol trisphosphate: A two-dimensional model. *Am J Physiol* 268(6 Pt 1):C1537–C1545.
74. Hubley MJ, Locke BR, Moerland TS (1996) The effects of temperature, pH, and magnesium on the diffusion coefficient of ATP in solutions of physiological ionic strength. *Biochim Biophys Acta* 1291(2):115–121.

# Supporting Information

Ceriani et al. 10.1073/pnas.1616061113

## General Description of the Computational Model

A schematic representation of the model is shown in Fig. 1. Letters  $J$  and  $K$ , both expressed in  $\mu\text{M}\cdot\text{s}^{-1}$ , indicate fluxes through channels/pumps and rate of production/degradation, respectively. Model parameters are summarized in Table S1. The model is composed of  $\text{Ca}^{2+}$ ,  $\text{IP}_3$ , and ATP subsystems, as described hereafter.

**Intracellular  $\text{Ca}^{2+}$  Regulation.** Intracellular  $\text{Ca}^{2+}$  levels can be modulated by a large variety of mechanisms, which include  $\text{Ca}^{2+}$  influx from the extracellular space or release from various intracellular stores (such as the endoplasmic/sarcoplasmic reticulum and mitochondria). However, our experimental data show that  $[\text{Ca}^{2+}]_c$  oscillations in cochlear nonsensory cells persist for tens of minutes even in the absence of extracellular  $\text{Ca}^{2+}$ . We thus neglected  $\text{Ca}^{2+}$  exchange through the plasma membrane, effectively reducing our model cell to a closed compartment in which the total intracellular free  $\text{Ca}^{2+}$  concentration ( $[\text{Ca}^{2+}]_{\text{tot}}$ ) is constant. We considered  $\text{IP}_3$ -dependent  $\text{Ca}^{2+}$  release from the ER as the only mechanism responsible for the observed changes of the  $[\text{Ca}^{2+}]_c$ , akin to similar models of  $\text{Ca}^{2+}$  dynamics in nonexcitable cells (67–69). Treating the cell cytoplasm as a well stirred compartment, the continuity equation for  $\text{Ca}^{2+}$  reads

$$\frac{d[\text{Ca}^{2+}]_c}{dt} = J_{\text{rel}} + J_{\text{leak}} - J_{\text{serca}}, \quad [\text{S1}]$$

where  $J_{\text{rel}}$  is the rate of change of  $[\text{Ca}^{2+}]_c$  due to the ( $\text{IP}_3$ -dependent)  $\text{Ca}^{2+}$  release from the ER through  $\text{IP}_3$  receptors ( $\text{IP}_3\text{Rs}$ ),  $J_{\text{leak}}$  is the rate of ( $\text{IP}_3$ -independent)  $\text{Ca}^{2+}$  leakage from the ER, and  $J_{\text{serca}}$  is the rate of  $\text{Ca}^{2+}$  clearance due to uptake into the ER by sarco/endoplasmic reticulum  $\text{Ca}^{2+}$ -ATPase (SERCA pumps).

The  $\text{Ca}^{2+}$  concentration in the ER ( $[\text{Ca}^{2+}]_{\text{ER}}$ ) is linked to that of the cytosol ( $[\text{Ca}^{2+}]_c$ ) by the conservation equation

$$\alpha \cdot [\text{Ca}^{2+}]_{\text{ER}} = [\text{Ca}^{2+}]_{\text{TOT}} - [\text{Ca}^{2+}]_c, \quad [\text{S2}]$$

where  $\alpha$  denotes the ratio of ER to cytosol volume. We described the SERCA pump rate as a Hill function of  $[\text{Ca}^{2+}]_c$  with exponent 2,

$$J_{\text{serca}} = v_{\text{serca}} \frac{([\text{Ca}^{2+}]_c)^2}{([\text{Ca}^{2+}]_c)^2 + k_{\text{serca}}^2}, \quad [\text{S3}]$$

where  $v_{\text{serca}}$  is the maximum rate of the pump and  $k_{\text{serca}}$  its  $\text{Ca}^{2+}$  affinity (70). The leakage rate was assumed to be proportional to the concentration difference between the ER and the cytosol:

$$J_{\text{leak}} = r_{\text{leak}} ([\text{Ca}^{2+}]_{\text{ER}} - [\text{Ca}^{2+}]_c). \quad [\text{S4}]$$

The rate of  $\text{Ca}^{2+}$  release through  $\text{IP}_3\text{R}$  is described by the equation

$$J_{\text{rel}} = r_{\text{rel}} P_{\text{IP}_3\text{R}} \cdot ([\text{Ca}^{2+}]_{\text{ER}} - [\text{Ca}^{2+}]_c), \quad [\text{S5}]$$

where  $r_{\text{rel}}$  is the maximum rate of release and  $P_{\text{IP}_3\text{R}}$ , the open probability of the  $\text{IP}_3\text{R}$ , is given by

$$P_{\text{IP}_3\text{R}} = m^3 n^3 [h(t)]^3. \quad [\text{S6}]$$

$m$ ,  $n$ , and  $h$  (with values between 0 and 1) are the three adimensional variables of the DeYoung–Keizer model (67), which account for  $\text{IP}_3$  binding, activation by  $\text{Ca}^{2+}$ , and inactivation by  $\text{Ca}^{2+}$  of the  $\text{IP}_3\text{R}$ , respectively.

In the Li–Rinzel reduction of the DeYoung–Keizer model (71), which we adopt here,  $\text{IP}_3$  binding and activation by  $\text{Ca}^{2+}$  are assumed to occur on a faster time scale than  $\text{Ca}^{2+}$  inactivation. Consequently  $m$  and  $n$  are assumed to be in instantaneous equilibrium (hence the  $\infty$  subscript in Eq. S6) and to obey a Hill function of the intracellular  $[\text{IP}_3]_c$  with affinity  $d_1$  and  $[\text{Ca}^{2+}]_c$  with affinity  $d_5$ , respectively:

$$m_\infty = \frac{[\text{IP}_3]_c}{[\text{IP}_3]_c + d_1} \quad [\text{S7}]$$

$$n_\infty = \frac{[\text{Ca}^{2+}]_c}{[\text{Ca}^{2+}]_c + d_5}. \quad [\text{S8}]$$

Finally, the time-dependent, Hodgkin and Huxley-like variable  $h$  is a solution to the differential equation

$$\frac{dh}{dt} = \frac{h_\infty - h}{\tau_h}, \quad [\text{S9}]$$

where

$$\tau_h = \frac{1}{a_2(Q_2 + [\text{Ca}^{2+}]_c)} \quad [\text{S10}]$$

$$h_\infty = \frac{Q_2}{Q_2 + [\text{Ca}^{2+}]_c} \quad [\text{S11}]$$

$$Q_2 = d_2 \frac{[\text{IP}_3]_c + d_1}{[\text{IP}_3]_c + d_3}. \quad [\text{S12}]$$

Parameters  $d_1$ ,  $d_3$ , and  $d_5$  and the power of 3 in Eq. S6 were selected by DeYoung and Keizer to fit the steady-state open probability of the  $\text{IP}_3\text{R}$  measured experimentally by Bezprozvany et al. (42).

In summary, the balance of cytosolic  $\text{Ca}^{2+}$  is dictated by Eq. S9 and the following equation:

$$\begin{aligned} \frac{d[\text{Ca}^{2+}]_c}{dt} = & (r_{\text{rel}} \cdot m_\infty^3 n_\infty^3 [h(t)]^3 + r_{\text{leak}}) ([\text{Ca}^{2+}]_{\text{ER}} - [\text{Ca}^{2+}]_c) \\ & - v_{\text{serca}} \frac{([\text{Ca}^{2+}]_c)^2}{([\text{Ca}^{2+}]_c)^2 + (k_{\text{serca}})^2}. \end{aligned} \quad [\text{S13}]$$

**$\text{IP}_3$  Regulation.** The dynamics of  $\text{IP}_3$  are described by the equation

$$\frac{d[\text{IP}_3]_c}{dt} = K_{\text{PLC}} - K_{\text{deg}}^{\text{IP}_3} + J_{\text{GJ}}^{\text{IP}_3}, \quad [\text{S14}]$$

where  $K_{\text{PLC}}$  indicates the rate of  $\text{IP}_3$  production due to phospholipase-C activity,  $K_{\text{deg}}^{\text{IP}_3}$  indicates  $\text{IP}_3$  degradation, and  $J_{\text{GJ}}^{\text{IP}_3}$  is the

rate of change of  $[IP_3]_c$  due to the intercellular flux from adjacent cells through gap junction channels. To limit the number of variables, we assumed  $K_{PLC}$  to be a Hill function of the  $[ATP]_e$ ,

$$K_{PLC} = v_{PLC} \frac{([ATP]_e)^{n_{PLC}}}{([ATP]_e)^{n_{PLC}} + (k_{PLC})^{n_{PLC}}}, \quad [S15]$$

where  $v_{PLC}$ ,  $n_{PLC}$ , and  $k_{PLC}$  are empirically fitted parameters (Table S1).

To take into account the observed time-dependent rundown of  $[Ca^{2+}]_c$  responses at high  $[ATP]_e$ , we assumed  $v_{PLC}$  to obey the following differential equation for  $[ATP]_e$  concentrations above  $1 \mu M$ ,

$$\frac{dv_{PLC}}{dt} = -\frac{1}{\tau_{PLC}} \cdot v_{PLC}, \quad [S16]$$

where

$$\tau_{PLC} = A_1 \cdot e^{-A_2 \cdot [ATP]_e} + A_3 \quad [S17]$$

and  $A_1, A_2, A_3$  are empirically fitted parameters.

A more comprehensive mathematical description of agonist-dependent  $IP_3$  production is provided in ref. 72.

As for  $K_{deg}^{IP_3}$  and  $J_{GJ}^{IP_3}$ , following Sneyd et al. (73) we modeled  $IP_3$  degradation rate as a linear function of  $[IP_3]_c$ ,

$$K_{deg}^{IP_3} = r_{deg}^{IP_3} [IP_3]_c, \quad [S18]$$

whereas the intercellular flux of  $IP_3$  between each pair of neighboring cells was assumed to be proportional to the difference of  $[IP_3]_c$  between them,

$$J_{GJ}^{IP_3} = k_j \cdot \sum_{\langle i,j \rangle} ([IP_3]_{c,i} - [IP_3]_c), \quad [S19]$$

where  $\sum_{\langle i,j \rangle}$  indicates sum over all nearest neighboring cells (Fig. S1) and  $[IP_3]_{c,i}$  indicates the cytosolic  $IP_3$  concentration in the  $i$ th neighbor. The  $IP_3$  junctional transfer rate

$$k_j = p_u \frac{N_{ch}}{V} \quad [S20]$$

depends on the number of channels,  $N_{ch}$ , their unitary permeability to  $IP_3$ ,  $p_u$ , and the volume of the cell,  $V$  (44).

To simulate  $[IP_3]_c$  oscillations in Figs. S2–S4, Eq. S14 was replaced by the time-dependent function

$$[IP_3]_c = C + A \cdot \sin(2\pi ft), \quad [S21]$$

where  $A$ ,  $f$ , and  $C$  are the oscillation amplitude, frequency, and tonic component, respectively.

**ATP Release and Diffusion Through the Extracellular Space.** As mentioned above, a key component of  $Ca^{2+}$  signaling in cochlear nonsensory cells is extracellular ATP, which is released through connexin hemichannels at the endolymphatic surface of the sensory epithelium and is degraded by ectonucleotidases. To describe the effects of ATP, we used the following reaction diffusion equation:

$$\frac{\partial [ATP]_e}{\partial t} = D \nabla^2 [ATP]_e + J_{ATP} - K_{deg}^{ATP}. \quad [S22]$$

The first term on the right-hand side accounts for ATP diffusion in the extracellular space.  $D$  is the diffusion coefficient of ATP in

the extracellular medium,  $\nabla^2$  is the Laplacian operator in space,  $J_{ATP}$  represents the efflux of ATP from cytosol into endolymph through connexin hemichannels, and  $K_{deg}^{ATP}$  represents the rate of ATP degradation by ectonucleotidases at the endolymphatic surface of the sensory epithelium. Akin to Eq. S18, we modeled ATP degradation rate as a linear function of the  $[ATP]_e$ :

$$K_{deg}^{ATP} = r_{deg}^{ATP} [ATP]_e. \quad [S23]$$

$J_{ATP}$  was assumed to be proportional to hemichannel open probability,  $P_{HC}$ , according to the equation

$$J_{ATP} = v_{HC} P_{HC}. \quad [S24]$$

To account for the experimentally determined bell-shaped dependence of  $P_{HC}$  on  $[Ca^{2+}]_c$  (Fig. 1C), we formulated the four-state model described in Fig. 1B. Each state is indicated as  $S_{ij}$ , where  $i = 0, 1$  indicates  $Ca^{2+}$  binding to a putative activating site and  $j = 0, 1$  indicates  $Ca^{2+}$  binding to a putative inactivating site. We also assumed the rate of  $Ca^{2+}$  binding to the activating site to be independent from  $Ca^{2+}$  presence at the inactivating site and vice versa (four rate constants): The channel is open if  $Ca^{2+}$  is bound to the activating site and not bound to the inactivating site (state  $S_{1,0}$ ).

Thus, denoting with  $x_{ij}$  the fraction of channel subunits in the state  $S_{ij}$ , the scheme in Fig. 1B is equivalent to the following set of equations,

$$\frac{dx_{0,0}}{dt} = -k_1 [Ca^{2+}]_c \cdot x_{0,0} + k_{-1} \cdot x_{0,1} - k_2 [Ca^{2+}]_c \cdot x_{0,0} + k_{-2} \cdot x_{1,0} \quad [S25]$$

$$\frac{dx_{1,0}}{dt} = -k_1 [Ca^{2+}]_c \cdot x_{1,0} + k_{-1} \cdot x_{1,1} + k_2 [Ca^{2+}]_c \cdot x_{0,0} - k_{-2} \cdot x_{1,0} \quad [S26]$$

$$\frac{dx_{0,1}}{dt} = k_1 [Ca^{2+}]_c \cdot x_{0,0} - k_{-1} \cdot x_{0,1} - k_2 [Ca^{2+}]_c \cdot x_{0,1} + k_{-2} \cdot x_{1,1} \quad [S27]$$

$$x_{1,1} = 1 - (x_{0,0} + x_{1,0} + x_{0,1}), \quad [S28]$$

and the open probability is given by

$$P_{HC} = \beta \cdot (x_{1,0})^{\gamma}, \quad [S29]$$

where  $\beta$  is a normalization constant. Values for the other parameters in Eqs. S25–S29 (Table S1) were selected by fitting the data of De Vuyst et al. (22) (Fig. 1B).

We solved the above set of time-dependent ordinary differential equations iteratively, using Euler's method with time step  $\Delta t = 1$  ms. The partial differential Eq. S22 was solved using a finite difference approach with a time step  $\Delta t = 0.1$  ms. The domain volume (a cube with  $281\text{-}\mu m$  sides) was divided into cubic voxels with  $3\text{-}\mu m$  sides and the endolymphatic surfaces of epithelial cells were modeled as polygons in the  $z = 0\text{-}\mu m$  plane. A reflecting boundary was introduced at  $z = 0 \mu m$  to reproduce the presence of the epithelium. A reflecting boundary was also imposed at the level of the hair cell region to account for the 3D shape of the organ of Corti. Absorbing boundaries were imposed at all other faces of the cubic domain volume.

### Number of Open Hemichannels That Contribute to ATP Release from a Given Cell

Estimating the number of open hemichannels that release ATP,  $N_{HC}$ , is more difficult than estimating the number of gap junction

channels between supporting cells mainly because the unitary permeability of hemichannels to ATP is not known (we can call it  $p_{\text{HC}}$ ). We can attempt to estimate  $N_{\text{HC}}$  by finding a link with the maximal ATP release rate of the model,  $v_{\text{HC}}$  ( $\text{mol}\cdot\text{L}^{-1}\cdot\text{s}^{-1}$ ).

Let  $dm$  denote the net molar amount of ATP released during a time interval  $dt$  from a single cell. Conservation of mass requires that

$$dm/dt = N_{\text{HC}} J_{\text{HC}}. \quad [\text{S30}]$$

$J_{\text{HC}}$  ( $\text{mol}\cdot\text{s}^{-1}$ ) is the net flux of ATP through a single hemichannel and is given by

$$J_{\text{HC}} = p_{\text{HC}} \Delta c. \quad [\text{S31}]$$

The units of  $p_{\text{HC}}$ , the unitary permeability of hemichannels to ATP, are  $\mu\text{m}^3\cdot\text{s}^{-1}$  and the ATP concentration difference from the inside to the outside of the cell,  $\Delta c$ , is in the millimolar range.

Assuming that the ATP released by a given cell binds the extracellular domain of P2Y receptors only within a thin “effective volume”  $V_{\text{eff}}$  above the surface of the cell, we set

$$dm/dt = v_{\text{HC}} V_{\text{eff}}. \quad [\text{S32}]$$

Combining the above equations and solving for  $N_{\text{HC}}$  yields

$$N_{\text{HC}} = \frac{v_{\text{HC}} V_{\text{eff}}}{p_{\text{HC}} \Delta c}. \quad [\text{S33}]$$

To derive numerical values for  $N_{\text{HC}}$  from Eq. S33, we need to assign numerical values to each parameter on the right-hand side. We formulated the following hypotheses: (i) Acceptable  $v_{\text{HC}}$  values are those that generate model wave speeds in the range 13–17  $\mu\text{m}/\text{s}$  determined experimentally, i.e.,  $300 \mu\text{M}\cdot\text{s}^{-1} \leq v_{\text{HC}} \leq 2,000 \mu\text{M}\cdot\text{s}^{-1}$ ; (ii)  $\Delta c = 1,000 \mu\text{M}$  (order of magnitude); (iii)  $p_{\text{HC}}$  is similar to the unitary permeability  $p_u$  to  $\text{IP}_3$  of the full gap junction channel ( $72 \times 10^{-3} \mu\text{m}^3\cdot\text{s}^{-1}$ ; ref. 44); and (iv)  $V_{\text{eff}}$  is given by the area of the cell exposed to endolymph ( $\sim 200 \mu\text{m}^2$ ) times an effective height of 10 nm (0.01  $\mu\text{m}$ ) above it (order of magnitude).

If these hypotheses are correct, then  $N_{\text{HC}}$  is between 8 ( $v_{\text{HC}} = 300 \mu\text{M}\cdot\text{s}^{-1}$ ) and 55 ( $v_{\text{HC}} = 2,000 \mu\text{M}\cdot\text{s}^{-1}$ ). Given the uncertainty that affects most parameters in Eq. S33, a more relaxed estimate is probably  $10 \leq N_{\text{HC}} \leq 100$ .

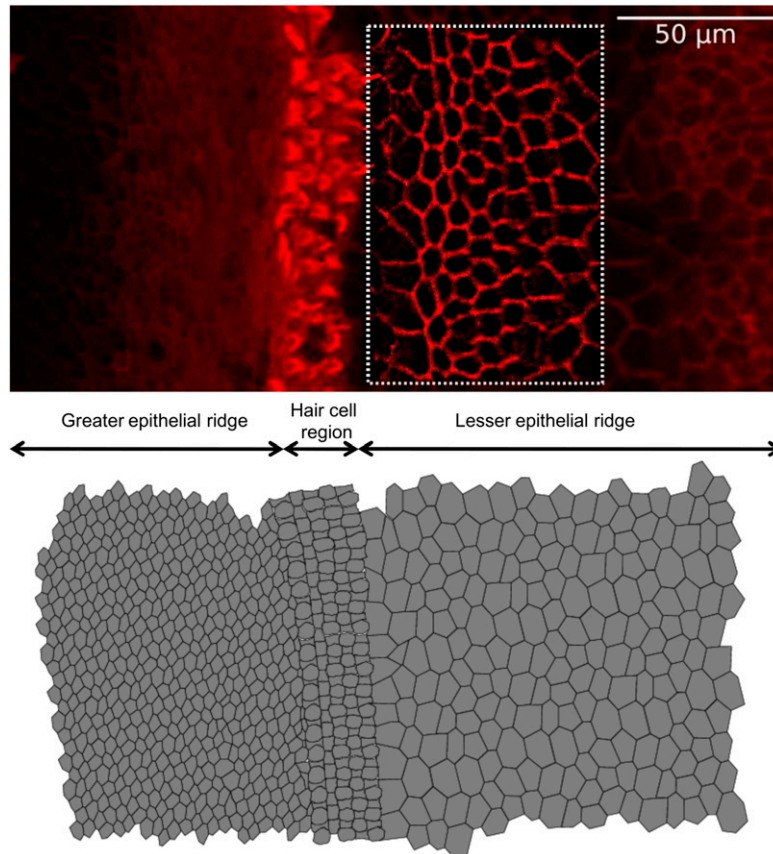


**Fig. S1.** Construction of realistic tissue morphology from confocal fluorescence imaging of a cochlear organotypic culture. (Top) Representative surface view of the cochlear sensory epithelium in an organotypic culture (P5, mouse). Image contrast was enhanced by application of an unsharp mask filter and an edge detection algorithm. (Bottom) Digitally reconstructed epithelium. The set of differential equations (*General Description of the Computational Model*) was solved iteratively for each cell in the network and intercellular diffusion of  $\text{IP}_3$  was computed for each pair of neighboring cells. Methods: Cochlear organotypic cultures were fixed in 4% paraformaldehyde for 20 min at room temperature and rinsed in PBS containing 2% BSA. F-Actin was stained for 1 h at room temperature with Texas Red-X phalloidin (ThermoFisher Scientific, no. T7471). After being washed three times in rinse solution, samples were mounted onto glass slides with a mounting medium (FluorSave Reagent; Merck, no. 345789). Images were acquired using a laser scanning confocal microscope (SP5; Leica).



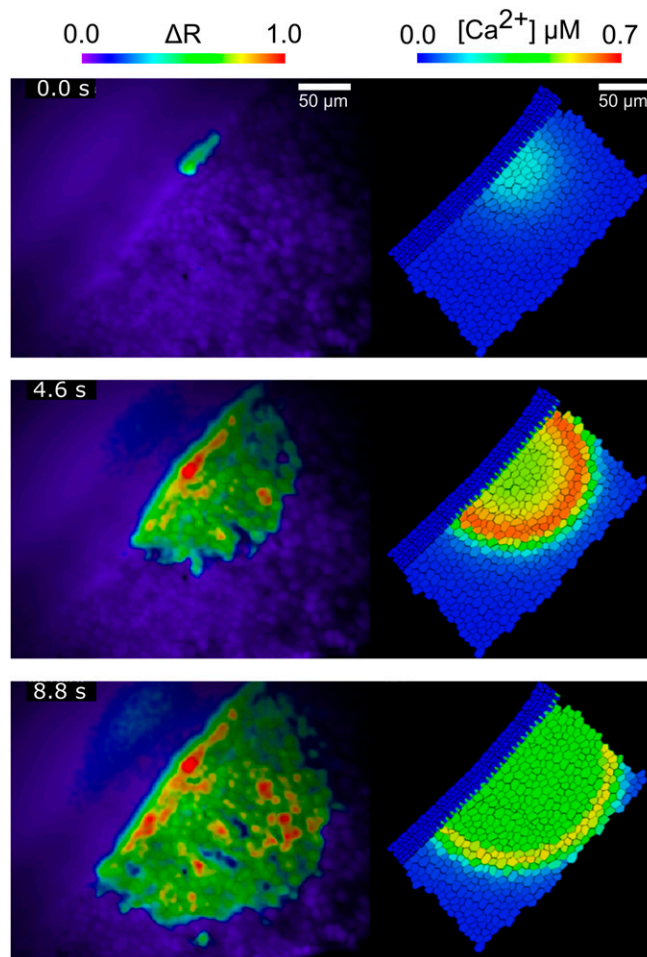






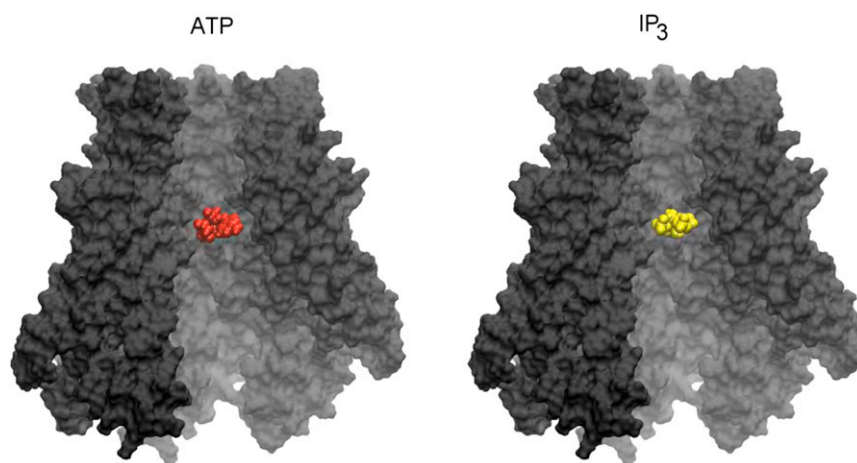
**Table S1. List of model parameters**

| Parameter                       | Unit                      | Description  | Value               | Source                      |
|---------------------------------|---------------------------|--|---------------------|-----------------------------|
| <b>Li-Rinzel model</b>          |                           |  |                     |                             |
| $r_{rel}$                       | $s^{-1}$                  | Maximal rate of $Ca^{2+}$ release                                      | 1.11                | (67)                        |
| $r_{leak}$                      | $s^{-1}$                  | Maximal rate of $Ca^{2+}$ leak   | 0.02035             | (67)                        |
| $v_{serca}$                     | $\mu M \cdot s^{-1}$      | Maximal rate of SERCA pumps  | 0.9                 | (67)                        |
| $k_{serca}$                     | $\mu M$                   | $Ca^{2+}$ affinity of SERCA pumps                                      | 0.11                | Fitted, Fig. 2B             |
| $d_1$                           | $\mu M$                   | Li-Rinzel model parameter  | 0.13                | (67)                        |
| $d_2$                           | $\mu M$                   | Li-Rinzel model parameter  | 1.049               | (67)                        |
| $d_3$                           | $\mu M$                   | Li-Rinzel model parameter  | 0.9434              | (67)                        |
| $d_5$                           | $\mu M$                   | Li-Rinzel model parameter  | 0.08234             | (67)                        |
| $a_2$                           | $\mu M^{-1} \cdot s^{-1}$ | Li-Rinzel model parameter  | 0.2                 | (67)                        |
| $\alpha$                        | —                         | Ratio between cytosol and ER volume                                    | 0.185               | (67)                        |
| $[Ca^{2+}]_{TOT}$               | $\mu M$                   | Total free $Ca^{2+}$ concentration                                     | 2                   | (67)                        |
| <b>IP<sub>3</sub> subsystem</b> |                           |  |                     |                             |
| $v_{PLC}$                       | $\mu M \cdot s^{-1}$      | Initial value of the maximal rate of IP <sub>3</sub> production by PLC | 0.101               | Fitted, Fig. 2B             |
| $k_{PLC}$                       | $\mu M$                   | ATP dissociation constant  | 0.038               | Fitted, Fig. 2B             |
| $n_{PLC}$                       | —                         | Hill exponent for ATP-dependent IP <sub>3</sub> production             | 0.28                | Fitted, Fig. 2B             |
| $r_{deg}^{IP_3}$                | $s^{-1}$                  | Rate of IP <sub>3</sub> degradation                                    | 0.13                | Fitted, Fig. 2B             |
| $\rho_u$                        | $\mu m^3 \cdot s^{-1}$    | Unitary IP <sub>3</sub> permeability of gap junction channels          | $72 \times 10^{-3}$ | (44)                        |
| $V$                             | $\mu m^3$                 | Cell volume  | 3,900               | Fitted, Fig. 2B             |
| $N_{ch}$                        | —                         | No. channels between two adjacent supporting cells                     | 935                 | Fitted, Fig. S2 and ref. 47 |
| $A_1$                           | s                         | $v_{PLC}$ time constant parameter                                      | 1,313               | Fitted                      |
| $A_2$                           | $\mu M^{-1}$              | $v_{PLC}$ time constant parameter                                      | 0.97                | Fitted                      |
| $A_3$                           | s                         | $v_{PLC}$ time constant parameter                                      | 46.66               | Fitted                      |
| <b>ATP subsystem</b>            |                           |  |                     |                             |
| $r_{deg}^{ATP}$                 | $s^{-1}$                  | ATP degradation rate   | 0.001–100           | Main text                   |
| $v_{HC}$                        | $\mu M \cdot s^{-1}$      | ATP maximal release rate   | 0–2000              | Main text                   |
| $D$                             | $\mu m^2 \cdot s^{-1}$    | ATP diffusion coefficient  | 363                 | (74)                        |
| $k_1$                           | $\mu M^{-1} \cdot s^{-1}$ | Hemichannel model constant   | 10.619              | Fitted, Fig. 1C             |
| $k_2$                           | $\mu M^{-1} \cdot s^{-1}$ | Hemichannel model constant   | 2.47                | Fitted, Fig. 1C             |
| $k_{-1}$                        | $s^{-1}$                  | Hemichannel model constant   | 3.4                 | Fitted, Fig. 1C             |
| $k_{-2}$                        | $s^{-1}$                  | Hemichannel model constant   | 2.38                | Fitted, Fig. 1C             |
| $\gamma$                        | —                         | Hemichannel model constant   | 9                   | Fitted, Fig. 1C             |



**Movie S1.** ATP-evoked radial  $\text{Ca}^{2+}$  wave: comparison between experiments (*Left*) and simulations (*Right*) (Fig. 6).

[Movie S1](#)



**Movie S2.** ATP and  $\text{IP}_3$  molecules in the pore of a homotypic connexin 26 hemichannel.

[Movie S2](#)